Tertiary Lymphoid Structure and CD8 T Cell Exclusion in Minimally Invasive Adenocarcinoma

Jin Wang[1], Dongbo Jiang[2], Xihao Hu[3], Xiaoqi Zheng[4], Wang Li[5], Tian Zhao[5], Di Wang[6], Huansha Yu[6], Dongqing Sun[1], Ziyi Li[1], Jian Zhang[7], Shengqing Gu[3], Zhe Zhang[8], Likun Hou[6], Gening Jiang[9], Fan Zhang[5], Kun Yang[2], Peng Zhang[9]

Affiliation

1. Clinical Translational Research Center, Shanghai Pulmonary Hospital, School of Life Sciences and Technology, Tongji University, Shanghai, China.
2. Department of Immunology, School of Basic Medicine, Air-Force Medical University. Xi'an, China.
3. Department of Data Science, Dana-Farber Cancer Institute, Harvard T.H. Chan School of Public Health, Boston, MA, USA.
4. Department of Mathematics, Shanghai Normal University, Shanghai, China.
5. Department of Thoracic Surgery, Shanghai Pulmonary Hospital, Tongji University School of Life Science and Technology, Shanghai, China.
6. Tissue Bank, Department of Pathology, Experimental Animal Center, Shanghai Pulmonary Hospital, Tongji University School of Medicine, Shanghai, China.
7. Center for Computational Biology, Beijing Institute of Basic Medical Sciences, Beijing, China.
8. Department of Gynecologic Oncology, Chinese PLA General Hospital, Beijing, China
9. Department of Thoracic Surgery, Shanghai Pulmonary Hospital, Tongji University School of Medicine, Shanghai, China.

Abstract

Lung adenocarcinoma is the leading cause of cancer death. To characterize the tumor microenvironment (TME) of early-stage lung adenocarcinoma, we performed RNA-seq profiling on 59 pairs of minimally invasive adenocarcinoma (MIA) tumors and matched adjacent normal lung tissues from Chinese patients. We observed mucin over-expression and glycosylation, and altered cytokine-cytokine interactions in MIA tumors, which also had distinct adaptive immune TME of higher CD4+ T cell infiltration, higher plasma B cell activation, and lower CD8+ T cell infiltration. The high expression of markers for B cells, activated CD4 T cells, and follicular helper T (Tfh) cells in MIA implicated the formation of tertiary lymphoid structures (TLS), which were supported by two independent single-cell RNA-seq data. Multiplex immunohistochemistry (mIHC) staining of 22 MIA tumors validated TLS formation and revealed an enrichment of follicular regulatory T cells (Tfr) in TLS follicles, which may explain the lower CD8+ T cell infiltration and attenuated anti-tumor immunity in MIA.

Significance: We discovered a potential immunosuppressive phenotype in MIA mediated by follicular regulatory T cells (Tfr) in TLS formation, which could be a potential mechanism of CD8+ T cell exclusion. Our study demonstrated how integrating tumor transcriptome and pathology can characterize the TME and elucidate potential mechanisms of tumor immune evasion.

Introduction

Lung cancer is the world's second-most common cancer but is by far the leading cause of cancer death. While most early lung cancer cases can be successfully treated, many lung cancers are not diagnosed until symptoms appear, at which time the disease has progressed to a more advanced stage. In recent years, low-dose computed tomography (LDCT) scan has been used for early lung cancer detection on people with a higher risk of lung cancer. Although LDCT has been shown to decrease the rate of lung cancer death, it also has a ~20% false-positive detection rate and exposes people to low-dose radiation (1). While these imaging approaches are promising, early detection and treatment of lung cancer might be complemented by molecular approaches that characterize pre-cancerous lesions and their surrounding microenvironment. To better characterize the molecular, cellular, and tissue changes that drive tumor development and progression in its earliest stages, National Cancer Institute of the United States has recently issued new initiatives to construct an atlas of pre-cancer lesions and their surrounding microenvironment. Following The Cancer Genome Atlas (TCGA) project which successfully profiled thousands of human cancers, this new effort promises to provide better understanding of cancer initiation and bring new strategies for cancer diagnosis and treatment.

Non-Small Cell Lung Cancer (NSCLC) accounts for about 80% of all lung cancer incidences, with a majority belonging to the adenocarcinoma subtype. Early lung adenocarcinoma development is believed to progress from adenocarcinoma in situ, to minimally invasive adenocarcinoma (MIA), then to fully invasive adenocarcinoma (2). Despite the difficulty of diagnosing early lung cancer lesions and obtaining samples, there have been a number of genomics studies on early lung cancers in recent years (2-5). For example, one study examined the mutation patterns of in situ and invasive adenocarcinoma by whole-exome sequencing and compared the results with TCGA (2). Another study used targeted sequencing and droplet PCR to examine the mutation patterns in both early tumors and the matched blood samples (3). Most of these studies focused on identifying driver mutations potentially responsible for tumor initiation, which have been summarized in a recent review (6).

Besides tumor mutations, there has been growing appreciations of the important roles tumor microenvironment (TME) plays in cancer development, progression, and outcome. The TME consists of cancer cells, tumor-infiltrating lymphocytes, stromal and vascular cells, along with extra-cellular molecules such as cytokines and chemokines that modulate their interactions. Changes in cellular and extra-cellular components of the TME can facilitate tumor behaviors such as unchecked tumor growth and immune evasion (7). To examine such TME changes, gene expression profiles from RNA-seq are more informative than DNA-based tumor profiling.

Besides characterizing differentially expressed genes and pathways, RNA-seq has reasonable power to detect somatic mutations (8), gene fusions (9) and microsatellite instability (10) , especially if matched normal samples are also available. There have also been multiple studies that use tumor RNA-seq data to infer immune cell populations and subtypes, and to associate immune infiltration with clinical outcomes or driver mutations (11,12). However, few such tumor profiling studies include matched adjacent tissues, and often the normal samples are sequenced at much lower coverage. One NSCLC study, which combined Whole Exome Sequencing (WES) and RNA-seq to discover the association between EGFR mutation and tumor-infiltrating B lymphocytes, did not profile RNA-seq from the matched normal, thus limiting the ability to characterize tumor-normal differences (13). Therefore, knowledge of the tumor immune microenvironment in early lung cancer patients, especially in comparison with the matched adjacent tissues, remains lacking.

In the TME, B cells and T cells are able to recognize and bind tumor antigens to induce adaptive immune responses (14,15). How cytotoxic T lymphocytes (CTL) influence immune response to tumor progression has been under intensive investigation in recent years (16). However, the role of B-T cell interactions in anti-tumor immune response has not been completely understood. Inflammation is known to be a potential cause and hallmark of early cancer development (17), and clusters of B and T lymphocytes can form tertiary lymphoid structure (TLS) at the site of inflammation(18). There has been increasing research interest in understanding TLS formation and function in human pathology, especially related to clinical implications and potential therapeutic targeting (19). A recent review summarized studies on the presence, composition, and functions of TLS in cancers and how TLS is correlated with therapeutic response (20). Three recent studies also reported TLS formation to be associated with response to immune checkpoint blockade (21-24). However, the impact of immune-stimulating or immune-suppressive components of TLS on tumor progression or immune evasion still awaits elucidation. Therefore, investigating TLS formation and its consequences on the tumor immune microenvironment in early stage tumors has the potential to inform disease etiology, precision medicine, and clinical prognosis.

In this study, we sought to characterize the TME of 59 pairs of minimally invasive adenocarcinoma (MIA) tumors and their matched adjacent normal tissues using RNA-seq. These tumors were initially diagnosed with LDCT, then surgically resected and confirmed for MIA by pathologists using hematoxylin and eosin (H&E) staining. To ensure an unbiased comparison between tumor and normal, we sequenced the RNA of both tumor and normal at higher depth than TCGA. This allowed us not only to examine the gene expression changes and infer immune cell infiltration levels, but also to compare the clonal expansion patterns of

the immune receptor repertoires between the tumors and the matched normal tissues. Furthermore, by combining transcriptome data, H&E staining, and multiplex immunohistochemistry (mIHC) staining on paraffin sections, we confirmed the TLS formation in the MIA TME, which might be associated with immune suppression and tumor initiation. These data and results provide insights into the etiology of early lung adenocarcinoma, which may inform immunotherapy treatment strategies for lung cancers.

128 # Results

129 **Genes in cytokine-cytokine receptor interactions and mucin glycosylation are over**
130 **expressed in MIA**

131 We collected 59 pairs of pathology-confirmed MIA tumors and matched adjacent normal
132 tissues **(Fig. S1, Table S1)**. All the MIA tumors were confirmed by pathology using the 2015
133 World Health Organization classification criteria of lung tumors (25). Hematoxylin and eosin
134 (H&E) staining confirmed the tumor lepidic growth pattern and the less than 5 mm in diameter
135 of invasive components **(Figure 1A)**. We conduced RNA-seq of all the samples at a minimum
136 depth of 100 million paired-end 150bp fragments, roughly three times the sequencing depth
137 of TCGA samples. We mapped the RNA-seq reads with STAR (26), quantified gene
138 expression with HTSeq (27), and called differentially expressed genes between paired tumor
139 and normal samples using edgeR (28). In total, we identified 1,471 up-regulated and 431
140 down-regulated genes with over 2-fold change and a false discovery rate (FDR) of less than
141 0.05 **(Table S2)**. We then applied gene set enrichment analysis (GSEA) (29) based on Kyoto
142 Encyclopedia of Genes and Genomes (KEGG) (30) to examine altered pathways in MIA
143 tumors **(Figure 1B)**. The most enriched up-regulated pathway in MIA is ABC-transporters
144 which has an established tumor-promoting role in regulating cell survival, proliferation,
145 migration, invasion, angiogenesis, and inflammation (31). In addition, widely studied cancer-
146 associated pathways, such as Ras signaling and PI3K-AKT signaling (32), are also
147 upregulated. Furthermore, MIA tumors exhibit stronger cytokine::cytokine-receptor
148 interactions than adjacent tissues. One particularly overexpressed cytokine, *CXCL13*,
149 encodes a chemokine that has been reported as a major B lymphocyte chemoattractant (33)
150 **(Fig. S2)**. Another pathway showing significant enrichment in MIA tumors is mucin-type O-
151 glycan biosynthesis. Many genes in the mucin family are over-expressed in MIA, especially
152 *MUC21*, *MUC5B*, and *MUC4* **(Figure 1C)**, a phenomenon also observed in TCGA lung
153 adenocarcinoma (LUAD) **(Fig. S3)**. Over-expression of mucin family proteins have been
154 reported to contribute to the carbohydrate-enriched coating of cancer cells, which could
155 promote integrin-mediated tumor growth and survival (34). In addition, overexpression and
156 glycosylation of mucins, especially of MUC1, have been reported in multiple cancers and
157 implicated to promote tumor metastasis and drug resistance (35,36). The overexpression of
158 mucin family members likely accounts for the enrichment of mucin-type O-glycan pathway in
159 MIA tumors.

160

161 **MIA tumors harbor EGFR and Mucin gene mutations**

162 We next sought to detect mutations in MIA tumors by comparing RNA-seq data between tumor
163 and adjacent normal tissue using Varscan2 (37). Although this is less sensitive than mutation

164 calling from DNA-based approaches such as whole genome or whole exome sequencing, we
165 still managed to find approximately 70 (median) variants per tumor, most of which were
166 missense mutations **(Fig. S4A)**. The most enriched type of single nucleotide variants (SNV)
167 is C>T transition **(Fig. S4B)**, which is known to be a signature of mismatch repair deficiency
168 resulting in elevated microsatellite instability (MSI) (38). To computationally assess the MSI
169 level of these MIA samples, we applied MSIsensor (10) to compare the RNA-seq data between
170 tumor and normal. Although this is also less sensitive than DNA-based approaches, we indeed
171 observed higher MSI score in MIA tumors with higher CT transition rate (**Fig. S4C**).
172
173 *EGFR* was found to be mutated in 31% of the MIA samples **(Figure 1D)**, consistent with the
174 previous report of the prevalent *EGFR* mutations in progressive stages of lung
175 adenocarcinoma (13). *EGFR* mutations occur mainly at the mutational hotspot "L858R/M" (39)
176 **(Figure 1E)** in the kinase domain, in agreement observations in TCGA LUAD **(Fig. S4D)**.
177 *EGFR* is known to participate in the signaling of the RTK-RAS pathway (32). The gain-of-
178 function EGFR mutations primarily contributed to the oncogenic activation of the RTK-RAS
179 pathway. Another important gene in the RTK-RAS pathway, *KRAS*, is mutated in only two
180 tumors (**Fig. S4E**), and as expected, occurs mutually exclusively with *EGFR* mutations (40).
181
182 In addition to RTK-RAS pathway mutations, *MUC6* and *MUC4* genes were also highly mutated
183 in MIA tumors. These two genes, as well as other MUC family members *MUC16*, *MUC5B* and
184 *MUC17*, are frequently mutated in TCGA LUAD **(Fig. S3)**. Most of the MUC family SNVs are
185 missense mutations, and together with their frequent over expression, suggest that tumor-
186 associated mucins might create neoantigens in MIA tumors. We therefore applied OptiType
187 (41) to infer the patient MHC Class I type and pVAC-Seq (42) to predict the likely neo-antigens
188 in these MIA tumors. Indeed, our analysis supports mutated MUC6, MUC4, MUC20 as being
189 potential neoantigens in MIA tumors (Fig. S5).
190
191 **Higher B cell and CD4+ T cell infiltration and activation but lower CD8+ T cell infiltration**
192 **in MIA tumors**
193 To decipher immune cell infiltration in the MIA TME, we estimated the immune cell composition
194 from bulk tumor RNA-seq data using TIMER (43), CIBERSORT (11). Relative to adjacent
195 normal tissues, MIA samples have significantly higher B cells and CD4+ T cells, and
196 significantly lower CD8+ T cells and macrophages **(Figure 2A and Fig. S6)**. Consistent with
197 the observation in MIA, TCGA LUAD tumors also showed higher B-cell and lower CD8+ T cell
198 infiltration in tumors than the adjacent normal tissues. Interestingly, B cell infiltration gradually
199 decreases towards normal during tumor progression from Stage I to Stage IV **(Figure 2B)** in
200 TCGA LUAD, suggesting that increased B cell increase is associated with early LUAD onset.

201 Next we characterized the immune repertoires in these samples to investigate the activation
202 and clonal expansion of tumor-infiltrating B and T cells. We ran TRUST, a computational
203 algorithm we developed (44,45), to assemble the T-cell and B-cell receptor (TCR and BCR)
204 repertoires from RNA-seq data. Significantly higher fractions of raw reads were mapped to
205 TCR and BCR in MIA tumors than normal tissues (**Fig S7A-B**). Consistent with this
206 observation, TRUST assembled significantly higher number TCR and BCR unique clonotypes
207 of Complementary Determining Region 3 (CDR3) sequences in MIA tumors (**Figure 2C-D**).
208 Since TRUST has better power to call the abundant and clonal-expanded TCRs and BCRs,
209 the fact that TRUST assembled more TCR/BCR clonotypes already suggest that T cells and
210 B cells have clonal expansion in the MIA tumors. Based on the CD4+ and CD8+ T cell
211 infiltration trend in MIA vs adjacent normal, we expect most of the T cell activation and clonal
212 expansion to occur in CD4+ T cells. Indeed, MIA tumors have significantly higher expression
213 of CD4+ T cell activation markers CD69, CD40LG, CD25 (IL2RA), and CD62 (SELL) (46-
214 49)(**Figure 2E**). However, since TCR diversity and clonality calculation could be confounded
215 since we couldn't distinguish TCRs from CD4+ vs CD8+ T cells, we turned to BCR to further
216 evaluate immune cell clonal expansion. For B cells, we not only observed higher total number
217 of BCR CDR3 clonotypes (**Figure 2D**) and BCR clusters (**Figure 2F**), but also lower BCR
218 diversity (**Figure 2G**) and higher BCR clonality (**Figure 2H**) in MIA than adjacent normal, which
219 strongly support B cell clonal expansion. In addition, B cells, upon antigen recognition and
220 clonal expansion, undergo somatic hype-mutation (SHM) to evolve BCRs with better antigen
221 binding affinity, and class-switch recombination (CSR) to transition to antibody-producing
222 plasma cells. Indeed, we also observed higher BCR SHM rate (**Figure 2I**), higher CSR (**Fig**
223 **S7C**) in MIA than adjacent normal, further supporting higher activated and clonal expanded B
224 cells.
225
226 To check whether the activated tumor-infiltrating B and T cells could generate more diverse
227 clonotypes for binding to different antigens in the TME, we compared the clonotypes detected
228 between tumors and adjacent normal tissues. Majorities of the BCR (58.6%, **Figure 3A**) or
229 TCR (57.8%) clonotypes were uniquely detected in tumors (**Figure 3B**), suggesting more B
230 cell and T cell infiltration and clonal expansion in MIA tumors. We measured the repertoire
231 similarity between each pair of MIA and adjacent tissue using Jaccard index (50,51), and found
232 within-individual repertoire similarity to be much higher than the across-patient repertoire
233 similarity (**Figure 3C**). Interestingly, the TCR and BCR similarities between tumor and normal
234 (**Figure 3C**) are correlated, suggesting that T cells and B cells have coordinated clonal
235 expansion in the MIA tumors. In addition, repertoire similarities among normal samples (N-N)
236 are higher than that among MIA samples (T-T) from differential patients (**Figure 3D**),
237 suggesting that tumor-specific antigens stimulate the expansion of different TCR and BCR

238 clones in different tumors. Furthermore, tumors with higher mutation burden, as inferred from
239 Varscan2, have significantly lower BCR (p-value < 0.01) and TCR (p-value < 0.001) repertoire
240 similarity between tumor and adjacent tissues (**Fig. 3E**). Collectively, these observations
241 suggest that TRUST-inferred immune receptor repertoires represent activated and clonal
242 expanded B cells and potentially CD4+ T cells for recognizing and binding to tumor antigens
243 in MIA.
244
245 **Mucin mutation and overexpression is associated with CD4+ T cell-mediated B cell**
246 **activation in MIA tumors**
247 Since B cells could be activated by direct antigen stimulation and interaction with CD4+ T cells,
248 we further checked how B cell activation was induced in MIA. It has been reported that MUC1
249 glycosylated peptides can induce MHCII-restricted B-T cell interactions (52). In addition, a
250 synthetic peptide from the MUC1 tandem repeat region was shown to be presented by MHCII
251 molecules which resulted in the initiation of T helper cell responses (53). In our MIA samples,
252 we observed a positive association between mucin level and MHCII level (**Figure 4A**), raising
253 the possibility that higher mucin expression in cancer cells might be associated with higher
254 MHCII presentation. In addition, CD40 and its ligand CD40L are well-known to mediate the
255 interaction between B cells and CD4+ T cells (54). We observed significant positive correlation
256 between CD40 and CD40L in MIA tumors **(Figure 4B)**, which suggests CD4+ T cell-mediated
257 B cell activation. The average level of CD40 and CD40L is associated with mucin expression
258 (**Figure 4C**). Furthermore, we observed MIA tumors with over-expressed mucins have higher
259 levels of IgG and IgA isotypes, suggesting higher level of B cell activation and transition to
260 plasma cells (**Figure 4D**). Taken together, these results implicate the potential interactions
261 between the mutation or overexpression on mucins, MHCII presentation to CD4+ T cells, and
262 B cell activation and plasma cell transition in MIA tumors.
263
264 To further investigate B cell activation among heterogeneous tumors, we characterized the
265 overall immune status among the MIA samples using five signatures derived from the TCGA
266 pan-cancer study (12). These signatures include “IFN-g” (representing IFN-g response),
267 “Lymphocyte” (representing overall lymphocyte infiltration by B and T cells), “Macrophage”
268 (representing the activation of macrophages/monocytes), “TGF-β” (representing TGF-β
269 response), and “Wound healing” (representing core serum response). These five signatures
270 seem to have correlated signals in the MIA tumors, so we used the average of the five to rank
271 the MIA tumors from “immune-low” to “immune-high” **(Figure 4E, Methods)**. The “immune-
272 high” tumors are associated with increased expression of MHCII (**Fig. S8A**) and mucins (**Fig.
273 S8B**). In addition, the “immune-high” tumors are also associated with increased expression of
274 CD40 (**Fig. S8C**) and CD40L (**Fig. S8D**), suggesting stronger interactions between B cells

275 and CD4+ T cells. Furthermore, “immune-high” tumors are associated with higher B cell
276 signals, such as IgG and IgA expression (**Fig. S8E-F**) and unique BCR clonotypes (**Fig. S8H**).
277 Collectively, our observations suggest that mucin expression is associated with CD4+ T cell-
278 mediated B cell activation in MIA adaptive immunity.
279
280 **Formation of tertiary lymphoid structure (TLS) in MIA tumors**
281 Previous literature (18) reported that B-cell and CD4+ T-cell aggregation could lead to the
282 formation of tertiary lymphoid structures (TLS). TLS starts from scattered B and T cell
283 aggregation, progresses to follicles with separate T-Zones and B-Zones, and finally matures
284 into ectopic germinal centers (EGC) with follicular dendritic cells (FDC) in the light-Zone for
285 better B cell activation (20) (**Figure 5A**). In the EGC of mature TLS, B cells activates somatic
286 hypermutations, isotype class-switches, and antibody production(19). So far our analysis
287 revealed higher B-cell and CD4+ T-cell infiltration, lower CD8+ T-cell infiltration **(Figure 2A)**,
288 and higher CD4+ T cell-mediated B cell activation **(Figure 3, Figure 4**) in MIA tumors. This
289 motivated us to examine the expression of typical TLS markers for evidence of TLS formation
290 in MIA. CD19 and MS4A1 (CD20), which are typical B-cell markers (55,56), were highly
291 expressed in MIA tumors. The ligand-receptor pair CXCL13 and CXCR5, which are
292 conventional indicators of follicles (57), were also significantly higher expressed in MIA tumors.
293 Furthermore, the ligand-receptor pair CCL19 and CCR7, which are important for promoting T
294 cell and B cell homing to lymphoid structures (58), were also highly expressed in tumors
295 **(Figure 5B)**. These six TLS markers were all positively correlated with TIMER-estimated B
296 cell and CD4+ T cell abundance but negatively correlated with CD8+ T cell abundance **(Figure**
297 **5B)**.
298
299 Besides the six TLS markers we evaluated above, another 12-chemokine gene signature has
300 also been proposed to predict the presence of TLS (59,60). We observed highly correlated
301 expression signals between our six TLS markers and the 12-chemokine signatures **(Fig. S9A)**.
302 As a result, the two approaches give concordant TLS predictions in MIA tumors, and found
303 TLS signals to be associated with immune-high tumors with stronger CD4+ T cell mediated B
304 cell activation **(Fig. S9B-C)**. To further confirm the presence of aggregated B cells and CD4+
305 T cells in non-small-cell lung cancer (NSCLC), we also examined two recently published
306 NSCLC single-cell RNA-seq datasets with tumors and adjacent normal tissues (61,62). Indeed,
307 NSCLC tumors have higher level of MS4A1+ B cells, CD4+CXCR5+ follicular helper T cells
308 (Tfh) than adjacent normal tissues (**Fig. S10A-B, Fig. S11A-B**). In addition, we used a
309 computational algorithm CellPhoneDB (63) infer cell–cell communication from combined
310 expression of multi-subunit ligand–receptor complexes to confirm the interaction between

311 CD40LG in CD4+ T cells with CD40 in B cells (**Fig. S11C**). Collectively, our MIA RNA-seq
312 data and NSCLC scRNA-seq data support TLS formation in lung adenocarcinoma (**Figure 4**).
313
314 With the transcriptome evidences of TLS formation in MIA tumors, we next sought to confirm
315 TLS formation from pathology imaging. Firstly, we examined the hematoxylin and Eosin
316 staining (H&E) pathology slides and observed lymphocytes aggregation **(Fig. S12),** which
317 support TLS formation in MIA tumors. Then, we used a six-marker multiplex
318 immunohistochemistry (mIHC) to stain for TLS in 22 MIA tumors with high Tfh phenotype,
319 which included the markers CD20 for B cells, CD4 and CXCR5 for follicular helper T cells (Tfh),
320 CD8 for CD8+ T cells, and CD35 for follicular dendritic cells (FDC) **(Figure 5C)**. mIHC
321 confirmed the formation of TLS in MIA tumors, although different samples showed varying
322 level of TLS maturation **(Fig. S13)**. In the samples with mature EGC, we observed TLS B-cell
323 zone (TLS-BZ) as marked by CD20, TLS T-cell zone (TLS-TZ) as marked by CD4, and EGC
324 light zone (EGC-LZ) as marked by CD20, CD4, CXCR5, and CD35 **(Figure 5C, Fig. S14, Fig.**
325 **S15)**. Furthermore, we segmented each observation field into different areas
326 (Adenocarcinoma tissue, Non-Follicle, TLS T zone, TLS B zone, EGC light zone) to quantify
327 and compare the immune cell density between TLS follicles and non-follicle areas. Here TLS
328 follicle area includes TLS-TZ, TLS-BZ, and EGC-LZ, and non-follicle area includes scattered
329 T cells and B cells outside of TLS. In MIA tumors, CD20+ B cells (**Figure 5D**, p-value < 0.0001),
330 CD4+ T cells (**Figure 5E**, p-value < 0.0001) and CD35+ FDC (**Figure 5F,** p-value < 0.0001)
331 were significantly higher in TLS than in non-follicular area. In contrast, CD8+ T cell showed
332 significantly lower density (p-value < 0.0001) in TLS follicles than in non-follicle areas **(Figure**
333 **5G)**.
334
335 **Treg recruitment as potential mechanism of CD8+ T cell exclusion in tertiary lymphoid**
336 **structures**
337 Our transcriptome and mIHC data indicated that MIA tumors had lower CD8+ T cell infiltration
338 (**Figure 2A**) and lower CD8+ T cell density in TLS (**Figure 5G**), respectively. In addition, MIA
339 tumors have lower PD-L1 (CD274) expression than adjacent normal, suggesting PD-L1
340 independent mechanisms for CD8+ T cell suppression **(Fig. S16)**. This prompted us to explore
341 the potential mechanism of CD8+ T cell exclusion in TLS and MIA. We examined immune
342 suppressive cells, such as Tregs, M2 macrophages, neutrophils, monocytes, and fibroblasts
343 (64) for possible cause of CD8+ T cell exclusion. Most suppressive cells were lower in MIA
344 tumors than adjacent normal, with the exception of Treg cells (**Figure 6A**), suggesting a Treg-
345 mediated CD8 T cell exclusion. From two independent scRNA-seq datasets, we also observed
346 CD4+CXCR5+FOXP3+ follicular T regulatory (Tfr) cells to be enriched in NSCLC tumors (**Fig.**
347 **S10B, Fig. S11B**). These data suggest that Treg cells might be responsible to suppress CD8+

348 T cell infiltration in the region of lymphocyte aggregations **(Figure 4)**. To quantify the degree
349 of immune suppression over immune stimulation, we measured the ratio of follicular regulatory
350 T cells (Tfr) to follicular helper T cells (Tfh) in TLS by the normalized expression of three pairs
351 of phenotype markers for Tfr and Tfh cells (FOXP3 over BCL6, PDCD1 over ICOS, and IL2RA
352 over IL7R) (65), respectively. For each pair of markers, the ratio of Tfr / Tfh was negatively
353 associated with CD8+ T cell infiltration **(Figure 6B)**, suggesting that Tfr in TLS might have
354 negative effects on CD8+ T cell infiltration in MIA.
355
356 To further quantify the Tfr and Tfh in TLS, we used seven-marker mIHC staining on sequential
357 slides of 22 MIA samples with high TLS expression markers. Specifically, we used CD3, CD4,
358 CXCR5, and FOXP3 to detect Tfr cells and CD3, CD4, CXCR5, and BCL-6 to detect Tfh cells
359 **(Figure 6C)**, respectively. Within the 69 available observation fields from the 22 MIA tumors,
360 we found lower CD8+ T cell density in TLS follicles than non-follicular areas **(Figure 6D,** $P <$
361 0.0001**)**, which was consistent with our observations in the six-plex mIHC panel **(Figure 5E)**.
362 In addition, we observed a higher ratio of regulatory T cells to helper T cells in TLS follicles
363 than in non-follicular areas **(Figure 6E,** $P = 0.0032$**),** indicating stronger immune suppression
364 mediated by Tfr cells in TLS. To determine how the balance between immune suppression
365 from Tfr and immune stimulation from Tfh influence CD8+ T cell infiltration in TLS, we split all
366 the observation fields into two groups based on the Tfr / Tfh ratio. While higher Tfr / Tfh ratio
367 was associated with lower CD8+ T cell density in TLS follicles **(Figure 6F)**, no such difference
368 was found in non-follicular areas **(Fig. S17)**. These results suggest TLS formation to be
369 associated with CD8+ T cell exclusion through Tfr mediated immune suppression.
370

371 ## Discussion
372
373 In this study, we characterized the tumor microenvironment (TME) of minimally invasive
374 adenocarcinomas (MIA) by integrating transcriptome data (molecular profiling, mutation
375 analysis, immune cell estimation, and immune repertoire inference) and pathology staining
376 (hematoxylin and eosin staining and multiplex immune-histochemistry). We observed varying
377 levels of TLS formation, from the initial T cells and B cell aggregates, to follicle formation, to
378 the mature ectopic germinal centers (EGC), in the MIA TME. Furthermore, we propose
379 follicular Treg (Tfr) cells in the TLS as a potential CD8+ T cell exclusion mechanism in MIA
380 tumors.
381
382 Our analysis revealed mucins in MIA samples to be highly mutated, over-expressed, and
383 highly glycosylated. Mucins synthesized by epithelial cells are well-known to undergo
384 glycosylation alterations during neoplasia (66-68). Aberrant glycosylation metabolism is
385 common in cancers and known to facilitate cell survival and proliferation (66). Mucin
386 overexpression may promote tumorigenicity and metastasis (66), which was proposed as an
387 independent predictor for poor prognosis in lung adenocarcinoma (34). Glycosylated tumor-
388 associated mucin peptides have been reported be bound by MHCII molecules and presented
389 by B cells, leading to the activation of CD4+ T cells which in turn activates B cells through
390 CD40-CD40L interactions (52,69). Our study identified higher tumor-infiltrating B cells and
391 CD4+ T cells in both MIA and TCGA lung adenocarcinoma. Moreover, MIA tumors exhibited
392 strong signals of B cell activation, somatic hyper-mutation and clonal expansion. Our
393 observation of the positive associations of mucins with MHCII, B cell activation, and CD40-
394 CD40L interactions potentially suggested mucin overexpression as a potential cause of CD4+
395 T cell-mediated B cell activation in MIA tumors. In addition, this CD4+ T cell-mediated B cell
396 activation seemed to be associated with “immune-high” tumors.
397
398 Our observation of tumor-infiltrating B and CD4+ T cells suggested lymphocyte aggregation
399 and TLS formation in the MIA TME. We therefore examined additional transcriptome and
400 pathology evidences of TLS formation in MIA tumors. From MIA transcriptome, we observed
401 up-regulation of six key TLS indicators (19,70) of B cell infiltration (CD19, CD20), follicle
402 phenotype (CXCR5, CXCL13), and lymphocyte homing (CCR7 and CCL19). The results were
403 corroborated using another 12-chemokine TLS signature (59,60). From pathology, we not only
404 observed lymphocyte aggregation in the H&E slides, but also confirmed the co-localization of
405 B cells, Tfh and FDC in TLS using six-panel mIHC. EGC are known to activate B cells for
406 somatic hypermutation, antibody affinity maturation, class switching, and antibody production
407 (71). We observed higher density of CD20+ B cells, CD4+ T cells, and CD35+ FDC, but lower

density of CD8+ T cells in TLS follicles than in non-follicular areas. This motivated us to investigate whether cells previously reported to suppress CD8 T cell infiltration, such as Tregs, M2 macrophage, neutrophils, monocytes, or fibroblasts (64), inhibit CD8+ T cell infiltration in MIA. Further examination of bulk RNA-seq on our MIA tumors implicated Treg as the culprit of CD8 T cell exclusion in MIA tumors. This hypothesis was supported by previous auto-immune studies in human and mouse (72-76). Using mIHC to evaluate the ratio between immune suppression (Tfr) and immune stimulation (Tfh), we found a negative association between the Tfr / Tfh ratio and CD8+ T cell infiltration, further supporting Tfr-mediated CD8+ T cell exclusion in MIA.

Controversy still exists regarding the impact of TLS on clinical prognosis. For example, TLS was reported to be associated with poor prognosis in human hepatocellular carcinoma (77) but good prognosis in colorectal cancer and breast cancer (78,79). In NSCLC cohorts, TLS in the tumors was observed to be associated with favorable prognosis (80-82), dependent on high CD8+ T cell and mature dendritic cell infiltration in the tumors, although we observed a negative association between TLS with CD8 T cell infiltration in MIA tumors. Intriguingly, recent studies also reported TLS to be associated with better response to immune checkpoint inhibitors in melanoma and sarcoma (21,22,24). These studies suggest that the discrepancies of TLS on clinical prognosis may be dependent on the cancer type and clinical contexts. Our observation that TLS formation could be associated with Tfr recruitment, CD8 T cell exclusion, and immune suppression have potentially important implications in cancer immunotherapy: while tumors with TLS and a predominant Tfh recruitment might directly respond to anti-PD1 treatment, those with TLS and a predominant Tfr recruitment might benefit from initial anti-CTLA4 treatment to deplete the Tregs before responding to anti-PD1 treatment. Our current study is still limited in sample size and statistical power, although another study on medRxiv reported similar findings in early lung cancers (83). Currently, our analysis only revealed associations without having functional validation of the causal effects. Therefore, future research and clinical studies are needed to fully elucidate the mechanism of CD8 T cell exclusion and explore better immunotherapy strategies in cancer.

Methods

Sample collection and RNA sequencing

All 118 samples were collected from 59 MIA patients at Pulmonary Hospital, Shanghai, China. All specimens were obtained from patients with appropriate consent from the relevant institutional review board. The clinical information of these patients was shown in **Table S**1. The RNA extraction procedure was compiled with standard protocols. DNA and RNA were collected from samples using AllPrep DNA/RNA Mini Kit (Qiagen, 80204, Germany). The cDNAs were synthesized and used to construct RNA libraries using NEBNext Ultra RNA Library Prep Kit (NEB, E7530, USA) and NEBNext Multiplex Oligos for Illumina (NEB, E7335, USA). The libraries were sequenced on the Illumina HiSeq2500 platform via a 2x150bp paired-end sequencing at Annoroad Gene Technology (Beijing, China). For each sample, more than 200M fragments were sequenced.

Gene profile processing of MIA RNA-Seq data

The transcriptome data were processed by the standard RNA-Seq pipeline. We performed sequence mapping by STAR alignment (26), reads quantifying by HT-Seq Count (27), and gene expression measurement by TPM converting from read count. Differential expression analysis on paired samples was performed using edgeR (28). Gene set enrichment analysis was performed using GSEA (29). Pathway categories are referred from KEGG website(https://www.genome.jp/kegg/pathway.html)

TCGA data downloading

For TCGA LUAD dataset, we downloaded gene expression data and mutation data from firebrowse (http://firebrowse.org).

Mutation calling from paired RNA-Seq data

Mutation detection from paired RNA-Seq data was analyzed by Varscan2. Somatic variants from Varscan2 (37) were annotated by Variant Effect Predictor(VEP) (84) and vcf2maf (https://github.com/mskcc/vcf2maf). Variants with low quality were removed based on the criteria which GDC pipeline recommends (https://docs.gdc.cancer.gov/Data/File_Formats/MAF_Format/). Mutation visualization was implemented by Maftools (85) and Complexheatmap (86).

472 **Normalization for altered mucin expression**
473 Z-score normalization of mRNA expression for patients was performed. One over-expressed
474 or down-expressed gene was expected to have a difference of at least two standard deviations
475 from the mean of expression in the reference samples.
476
477 **Immune infiltration estimation from RNA-seq data**
478 We applied Tumor IMmune Estimation Resource (TIMER) (43) to deconvolve the immune cell
479 components in the TME using TPM expression data. To ensure robust abundance estimation,
480 CIBERSORT (11) according to the predefined LM22 signature and XCELL (87) were both
481 used to estimate immune cell infiltration.
482
483 **The immune signature score for classifying "immune-low" and "immune-high" MIA**
484 **tumors**
485 From the pan-cancer paper (12), the immune signature data and the pre-trained scoring model
486 were downloaded from the CRI-iAtlas (https://github.com/CRI-iAtlas/shiny-iatlas/). Based on
487 the model, we computed the five representative immune signatures score from the expression
488 data, which was normalized by paired normal tissues and median-centered by gene level.
489 Then, we ranked MIA tumors from immune "low" to immune "high" based on the averaged
490 immune signature score.
491
492 **Definitions of BCR repertoire metrics**
493 We applied TRUST3 to infer the immune repertoire from bulk RNA-seq data (44,45).We
494 measured basic metrics to quantify immune repertoire and further performed paired
495 comparison of TCR and BCR repertoire between tumor and tumor-adjacent tissues. The
496 fraction of TCR or BCR reads was defined as the library size located in BCR loci, which is
497 normalized by total mapped reads (E1). The number of unique TCR or BCR CDR3 sequences
498 summarized the total unique CDR3 size. The number of TCR or BCR clonotypes per kilo reads
499 measures TCR or BCR diversity. In addition, B cells undergo clonal expansions with a high
500 rate of somatic hypermutation by single base substitutions in CDR3 sequences. Thus, we built
501 BCR lineages referred to the method of a previous study (45), which generates 8-mer CDR3
502 motifs and an upper triangular matrix of counting the substitutions between DNA sequences
503 from any two clonotypes in one BCR lineage to cluster partial and complete CDR3 sequences.
504 For each sample, BCR or TCR clonality is defined by Shanno entropy (E2) (88). Somatic
505 hypermutation rate was defined as the total count of harboring one base substitution
506 normalized by the total length of aligned DNA sequence (E3). Ig class switch recombination
507 (CSR) were built for the BCR clonotypes with different Ig isotypes from the same BCR lineage.
508 Any two Ig isotypes within the same cluster motif could be switched based on the specific

509 order, which is IgM, IgD, IgG3, IgG1, IgA1, IgG2, IgG4, IgE, IgA2 (89,90). Here we only remain
510 the Ig isotypes with abundance more than 1% and check CSR on IgG and IgA for measuring
511 B cell activation signal. The ratio of CSR was computed referring to the method in the previous
512 study (45). The equations are shown below.

513 $$Fraction\ of\ TCR\ or\ BCR\ reads = \frac{l}{M} \qquad (E1)$$

514 l denotes library size located in BCR loci; M denotes total mapped reads.

515 $$Clonality = 1 - \frac{-\sum_{i=1}^{n} p_i log2(p_i)}{log2(n)} \qquad (E2)$$

516 $$p_i = \frac{f_i}{\sum_{i=1}^{n} f_i}$$

517 n denotes total number of TCR clonotypes or total number of BCR clusters and non-clustered
518 clonotypes, f_i denotes clonal frequency for non-clustered clonotypes or clustered clonotypes.

519 $$SHM\ rate = \frac{\sum_{i=1}^{c} S_i}{\sum_{i=1}^{c} \max(L_i)} \qquad (E3)$$

520 c denotes the number of BCR clusters, S_i denotes the sum of clonotype pairs harboring one
521 base substitution, L_i denotes the max number of aligned non-gapped DNA sequence in one
522 cluster.
523

524 **Tumor purity evaluation**

525 Tumor purity was estimated by the algorithm of EPIC (91) (http://epic.gfellerlab.org), which is
526 designed for estimating the absolute fraction of immune cells and cancer cells simultaneously
527 from RNA-seq expression data. We selected "tumor infiltrating cells" as reference profile to
528 predict cell fractions.
529

530 **Single-cell RNA-seq data analysis**

531 Two independent single-cell RNA-seq datasets were collected from NSCLC cohorts with
532 tumors and adjacent normal tissues (GSE139555, EMTAB6149). Single-cell RNA-seq dataset
533 pre-processing was performed by the comprehensive pipeline MAESTRO (92) . Single cell
534 clustering and cell type annotation are available to be visualized in TISCH (http://tisch.comp-
535 genomics.org/). In the dataset of NSCLC_ GSE139555, only cells from tumor and normal
536 tissues were extracted from raw count data for comparing gene expression of cells between
537 tumor and normal. In the dataset of NSCLC_ EMTAB6149, cluster averaged expression data
538 was downloaded from the paper supplementary data due to no available tissue information on
539 cell barcode level. Cell-cell interaction analysis was inferred utilizing a public method
540 CellPhoneDB (63). Only receptor-ligand pairs significantly enriched in less than 5% of all cell-
541 cell interactions were exhibited for the cell interactions on B cells or T cells in the dot plot.

542

543 **Immunohistochemistry**

544 Slides at 4-μm thickness were cut from paraffin blocks from MIA biopsies (n=59) and paired
545 normal lung tissue. Slides were then stained for the interested markers in certain condition of
546 antigen retrieval and incubation (**Table S3**) with Dako Real kit according to IHC-P protocol.
547 Tonsil tissue were performed as control for staining optimization.

548

549 **Multiplex immune-histochemistry staining for lymphocyte infiltrating in MIA**

550 Twenty-two matched paraffin blocks of the 59 samples were processed through the 4-μm-
551 thick section, deparaffinization in xylene, rehydration in an ethanol gradient. Slides were
552 stained according to Opal 7-plex technology (PerkinElmer), yielding to the simultaneous
553 visualization of seven markers (containing DAPI for nucleus) on the same slide. During each
554 of the six cycles of staining, antigen retrieval (AR) was conducted via microwave treatment in
555 AR solution pH 6 or pH 9 (AR6 or AR9) suggested by IHC validation; blocking was followed
556 by instructions for 15 mins at room temperature (RT); and primary antibodies were then
557 incubated for 1 hr at RT or overnight at 4 ℃. Next, HRP labeled polymer goat anti-mouse and
558 rabbit antibodies were incubated at RT for 10 min followed by TSA opal fluorophores (Opal
559 520, Opal 540, Opal 570, Opal 620, Opal 650 or Opal 690) 10 min incubation. Microwave
560 treatment was performed to remove the antibody TSA complex at each cycle of staining with
561 AR solution (pH 9 or pH 6). Finally, all slides were counterstained with DAPI for 5 min and
562 enclosed in ProLong Antifade Mountant (Solarbio). The slides were scanned using the
563 PerkinElmer Mantra System, and the multispectral images obtained were unmixed using
564 spectral libraries that were previously built from images stained for each fluorophore (mono-
565 plex), using the inForm Advanced Image Analysis software (inForm 2.4.1 PerkinElmer).

566

567 **Multispectral image analysis for tumor microenvironment of MIA**

568 The entire area of the sections was stained, scanned, scored, and quantified. The scoring
569 protocol consisted of several automated steps: tissue categorization, cell segmentation, and
570 cell phenotyping. Using the integrated InForm image analysis software, multispectral images
571 that were representative of different samples were selected and used to train the InForm
572 software for categorization of the tissue into epithelium and stroma. Microinvasive epithelium
573 without infiltration was tagged as “ACC” for cancer cell of adenocarcinoma, while lymphocyte
574 infiltrating stroma area was further recognized as “Non-Fol”, “TLS-BZ” and “TLS-TZ”,
575 representing scattered lymphocytes infiltration, B-cell zone of TLS formation, and T-cell zone
576 of TLS formation. The settings learned from the training on the representative images from
577 different samples were saved within an algorithm, which enabled a batch analysis of all the
578 tissue slides. We designed six-plex TLS panel for TLS component cells and seven-plex Tfr/h

579 panel for suppressive/stimulatory immune cells. They were used on two sequential slides to
580 characterize the immune microenvironment of MIA lesions. The TLS panel included CD4, CD8,
581 CD20, CD35, DAPI, and CXCR5 while the Tfr/h panel included CD3, CD4, CD8, FOXP3, BCL-
582 6, DAPI, and CXCR5. The software classified the tumor (epithelial) and infiltrated stromal
583 regions. The classification was verified and approved by a certified pathologist (W.D.). For six-
584 plex mIHC panel, CD20+ B density is defined as the percentage of CD20+ cells in total
585 immune cells, including CD8+ cells, CD20+ cells, CD35+ cells, and CD4+ cells. Similarly,
586 CD4+ T density is defined as the percentage of CD4+ cells in total immune cells. CD35+
587 density is defined as the percentage of CD35+ cells in total immune cells and CD8+ T density
588 is defined as the percentage of CD8+ cells in total immune cells. For seven-plex mIHC panel,
589 we defined the regulatory T-cell phenotype with $CD3^{+}CD4^{+}CXCR5^{+}FOXP3^{+}$Tfr and
590 $CD3^{+}CD4^{+}CXCR5^{-}FOXP3^{+}$Treg and stimulatory T-cell phenotype with
591 $CD3^{+}CD4^{+}CXCR5^{+}FOXP3^{-}$Tfh and $CD3^{+}CD4^{+}CXCR5^{-}FOXP3^{-}$Th. Either cell densities or
592 absolute counts were enrolled for calculation.
593
594 **Statistical analysis**
595 For all the statistical test for comparing the difference between tumor and match adjacent
596 tissues, Mann–Whitney U test was used to evaluate the P values and $P< 0.05$ was considered
597 statistically significant. Multiple hypothesis correction was computed in the form of adjusted p-
598 value through the Benjamini-Hochberg procedure. The thresholds used in the differential
599 expression analysis were 2.0 for fold-change and 0.05 for the adjusted P value. Spearman's
600 rank correlation coefficient was presented as the association of two independent features. A
601 partial correlation test was used to measure the correlation between genes and immune cell
602 infiltration when corrected by tumor purity. All the statistical tests were implemented using the
603 R programming language.
604

Authors' Contributions

Conception and design: Jin Wang, Dongbo Jiang
Development of methodology: Jin Wang, Dongbo Jiang, Xihao Hu
Acquisition of data (acquired and managed patients, provided facilities): Peng Zhang, Gening Jiang, Fan Zhang, Wang Li, Tian Zhao
Analysis and interpretation of data (e.g., statistical analysis, biostatistics, computational analysis): Jin Wang, Xihao Hu, Dongbo Jiang, Xiaoqi Zheng, Jian Zhang, Dongqing Sun, Shengqing Gu, Zhe Zhang, Kun Yang
Writing and review the manuscript: Jin Wang, Dongbo Jiang, Xihao Hu, Ziyi Li, Kun Yang
Administrative, technical, or material support: Huansha Yu, Di Wang
Study supervision: Peng Zhang, Kun Yang

Competing Interests

No competing interests.

Acknowledgments

The authors acknowledge Dr. X. Shirley Liu in Dana-Farber Cancer Institute and Dr. Arlene Sharpe in Harvard Medical School for the helpful discussion and advice, to Drs. Jia Liang and Rongjian Su in Jinzhou Medical University, Mr. Wei Liu and fellows of the SKLBCE-PerkinElmer Center of Excellence, Beijing, China for their assistance on the mIHC experiments.
This work was supported by the National Natural Science Foundation of China (Grant No. 81872290, 81972172, and 81772763), the Shanghai Science and Technology Committee (No. 19XD1423200, 18140903900).

630 ## References

631 1. Pinsky PF. Assessing the benefits and harms of low-dose computed tomography
632 screening for lung cancer. Lung Cancer Manag **2014**;3(6):491-8 doi
633 10.2217/LMT.14.41.
634 2. Vinayanuwattikun C, Le Calvez-Kelm F, Abedi-Ardekani B, Zaridze D, Mukeria A,
635 Voegele C*, et al.* Elucidating Genomic Characteristics of Lung Cancer Progression
636 from In Situ to Invasive Adenocarcinoma. Sci Rep **2016**;6:31628 doi
637 10.1038/srep31628.
638 3. Izumchenko E, Chang X, Brait M, Fertig E, Kagohara LT, Bedi A*, et al.* Targeted
639 sequencing reveals clonal genetic changes in the progression of early lung neoplasms
640 and paired circulating DNA. Nat Commun **2015**;6:8258 doi 10.1038/ncomms9258.
641 4. Lavin Y, Kobayashi S, Leader A, Amir ED, Elefant N, Bigenwald C*, et al.* Innate
642 Immune Landscape in Early Lung Adenocarcinoma by Paired Single-Cell Analyses.
643 Cell **2017**;169(4):750-65 e17 doi 10.1016/j.cell.2017.04.014.
644 5. Mascaux C, Angelova M, Vasaturo A, Beane J, Hijazi K, Anthoine G*, et al.* Immune
645 evasion before tumour invasion in early lung squamous carcinogenesis. Nature
646 **2019**;571(7766):570-5 doi 10.1038/s41586-019-1330-0.
647 6. Inamura K. Clinicopathological Characteristics and Mutations Driving Development of
648 Early Lung Adenocarcinoma: Tumor Initiation and Progression. International Journal
649 of Molecular Sciences **2018**;19(4) doi 10.3390/ijms19041259.
650 7. Binnewies M, Roberts EW, Kersten K, Chan V, Fearon DF, Merad M*, et al.*
651 Understanding the tumor immune microenvironment (TIME) for effective therapy. Nat
652 Med **2018**;24(5):541-50 doi 10.1038/s41591-018-0014-x.
653 8. Graw S, Meier R, Minn K, Bloomer C, Godwin AK, Fridley B*, et al.* Robust gene
654 expression and mutation analyses of RNA-sequencing of formalin-fixed diagnostic
655 tumor samples. Sci Rep **2015**;5:12335 doi 10.1038/srep12335.
656 9. Heyer EE, Deveson IW, Wooi D, Selinger CI, Lyons RJ, Hayes VM*, et al.* Diagnosis of
657 fusion genes using targeted RNA sequencing. Nat Commun **2019**;10(1):1388 doi
658 10.1038/s41467-019-09374-9.
659 10. Niu B, Ye K, Zhang Q, Lu C, Xie M, McLellan MD*, et al.* MSIsensor: microsatellite
660 instability detection using paired tumor-normal sequence data. Bioinformatics
661 **2014**;30(7):1015-6 doi 10.1093/bioinformatics/btt755.
662 11. Newman AM, Liu CL, Green MR, Gentles AJ, Feng W, Xu Y*, et al.* Robust enumeration
663 of cell subsets from tissue expression profiles. Nat Methods **2015**;12(5):453-7 doi
664 10.1038/nmeth.3337.
665 12. Thorsson V, Gibbs DL, Brown SD, Wolf D, Bortone DS, Ou Yang T-H*, et al.* The
666 Immune Landscape of Cancer. Immunity **2018**;48(4):812-30.e14 doi
667 10.1016/j.immuni.2018.03.023.
668 13. Wang C, Yin R, Dai J, Gu Y, Cui S, Ma H*, et al.* Whole-genome sequencing reveals
669 genomic signatures associated with the inflammatory microenvironments in Chinese
670 NSCLC patients. Nat Commun **2018**;9(1):2054 doi 10.1038/s41467-018-04492-2.
671 14. Hennecke J, Wiley DC. T cell receptor-MHC interactions up close. Cell **2001**;104(1):1-
672 4 doi 10.1016/s0092-8674(01)00185-4.
673 15. Heesters BA, van der Poel CE, Das A, Carroll MC. Antigen Presentation to B Cells.
674 Trends in Immunology **2016**;37(12):844-54 doi 10.1016/j.it.2016.10.003.
675 16. Tscharke DC, Croft NP, Doherty PC, La Gruta NL. Sizing up the key determinants of
676 the CD8+ T cell response. Nature Reviews Immunology **2015**;15(11):705-16 doi
677 10.1038/nri3905.
678 17. Coussens LM, Werb Z. Inflammation and cancer. Nature **2002**;420(6917):860-7 doi
679 10.1038/nature01322.
680 18. Corsiero E, Nerviani A, Bombardieri M, Pitzalis C. Ectopic Lymphoid Structures:
681 Powerhouse of Autoimmunity. Front Immunol **2016**;7:430 doi
682 10.3389/fimmu.2016.00430.

683 19. Pitzalis C, Jones GW, Bombardieri M, Jones SA. Ectopic lymphoid-like structures in
684 infection, cancer and autoimmunity. Nat Rev Immunol **2014**;14(7):447-62 doi
685 10.1038/nri3700.
686 20. Sautès-Fridman C, Petitprez F, Calderaro J, Fridman WH. Tertiary lymphoid structures
687 in the era of cancer immunotherapy. Nature Reviews Cancer **2019**;19(6):307-25 doi
688 10.1038/s41568-019-0144-6.
689 21. Cabrita R, Lauss M, Sanna A, Donia M, Skaarup Larsen M, Mitra S*, et al.* Tertiary
690 lymphoid structures improve immunotherapy and survival in melanoma. Nature
691 **2020**;577(7791):561-5 doi 10.1038/s41586-019-1914-8.
692 22. Helmink BA, Reddy SM, Gao J, Zhang S, Basar R, Thakur R*, et al.* B cells and tertiary
693 lymphoid structures promote immunotherapy response. Nature **2020**;577(7791):549-
694 55 doi 10.1038/s41586-019-1922-8.
695 23. Bruno TC. New predictors for immunotherapy responses sharpen our view of the
696 tumour microenvironment. Nature **2020**;577(7791):474-6 doi 10.1038/d41586-019-
697 03943-0.
698 24. Petitprez F, de Reynies A, Keung EZ, Chen TW, Sun CM, Calderaro J*, et al.* B cells
699 are associated with survival and immunotherapy response in sarcoma. Nature
700 **2020**;577(7791):556-60 doi 10.1038/s41586-019-1906-8.
701 25. Travis WD, Brambilla E, Nicholson AG, Yatabe Y, Austin JHM, Beasley MB*, et al.* The
702 2015 World Health Organization Classification of Lung Tumors: Impact of Genetic,
703 Clinical and Radiologic Advances Since the 2004 Classification. J Thorac Oncol
704 **2015**;10(9):1243-60 doi 10.1097/JTO.0000000000000630.
705 26. Dobin A, Davis CA, Schlesinger F, Drenkow J, Zaleski C, Jha S*, et al.* STAR: ultrafast
706 universal RNA-seq aligner. Bioinformatics **2013**;29(1):15-21 doi
707 10.1093/bioinformatics/bts635.
708 27. Anders S, Pyl PT, Huber W. HTSeq--a Python framework to work with high-throughput
709 sequencing data. Bioinformatics **2015**;31(2):166-9 doi 10.1093/bioinformatics/btu638.
710 28. Robinson MD, McCarthy DJ, Smyth GK. edgeR: a Bioconductor package for
711 differential expression analysis of digital gene expression data. Bioinformatics
712 **2010**;26(1):139-40 doi 10.1093/bioinformatics/btp616.
713 29. Subramanian A, Tamayo P, Mootha VK, Mukherjee S, Ebert BL, Gillette MA*, et al.*
714 Gene set enrichment analysis: a knowledge-based approach for interpreting genome-
715 wide expression profiles. Proc Natl Acad Sci U S A **2005**;102(43):15545-50 doi
716 10.1073/pnas.0506580102.
717 30. Kanehisa M, Goto S. KEGG: kyoto encyclopedia of genes and genomes. Nucleic Acids
718 Res **2000**;28(1):27-30 doi 10.1093/nar/28.1.27.
719 31. Fletcher JI, Haber M, Henderson MJ, Norris MD. ABC transporters in cancer: more
720 than just drug efflux pumps. Nature Reviews Cancer **2010**;10(2):147-56 doi
721 10.1038/nrc2789.
722 32. Sanchez-Vega F, Mina M, Armenia J, Chatila WK, Luna A, La KC*, et al.* Oncogenic
723 Signaling Pathways in The Cancer Genome Atlas. Cell **2018**;173(2):321-37 e10 doi
724 10.1016/j.cell.2018.03.035.
725 33. Legler DF, Loetscher M, Roos RS, Clark-Lewis I, Baggiolini M, Moser B. B cell-
726 attracting chemokine 1, a human CXC chemokine expressed in lymphoid tissues,
727 selectively attracts B lymphocytes via BLR1/CXCR5. J Exp Med **1998**;187(4):655-60
728 doi 10.1084/jem.187.4.655.
729 34. Lakshmanan I, Ponnusamy MP, Macha MA, Haridas D, Majhi PD, Kaur S*, et al.* Mucins
730 in lung cancer: diagnostic, prognostic, and therapeutic implications. J Thorac Oncol
731 **2015**;10(1):19-27 doi 10.1097/JTO.0000000000000404.
732 35. Bouillez A, Adeegbe D, Jin C, Hu X, Tagde A, Alam M*, et al.* MUC1-C promotes the
733 suppressive immune microenvironment in non-small cell lung cancer.
734 Oncoimmunology **2017**;6(9):e1338998 doi 10.1080/2162402X.2017.1338998.
735 36. Maeda T, Hiraki M, Jin C, Rajabi H, Tagde A, Alam M*, et al.* MUC1-C Induces PD-L1
736 and Immune Evasion in Triple-Negative Breast Cancer. Cancer Res **2018**;78(1):205-
737 15 doi 10.1158/0008-5472.CAN-17-1636.

738 37. Koboldt DC, Zhang Q, Larson DE, Shen D, McLellan MD, Lin L*, et al.* VarScan 2:
739 somatic mutation and copy number alteration discovery in cancer by exome
740 sequencing. Genome Res **2012**;22(3):568-76 doi 10.1101/gr.129684.111.
741 38. Harris RS. Cancer mutation signatures, DNA damage mechanisms, and potential
742 clinical implications. Genome Med **2013**;5(9):87 doi 10.1186/gm490.
743 39. Paez JG, Janne PA, Lee JC, Tracy S, Greulich H, Gabriel S*, et al.* EGFR mutations in
744 lung cancer: correlation with clinical response to gefitinib therapy. Science
745 **2004**;304(5676):1497-500 doi 10.1126/science.1099314.
746 40. Li S, Li L, Zhu Y, Huang C, Qin Y, Liu H*, et al.* Coexistence of EGFR with KRAS, or
747 BRAF, or PIK3CA somatic mutations in lung cancer: a comprehensive mutation
748 profiling from 5125 Chinese cohorts. Br J Cancer **2014**;110(11):2812-20 doi
749 10.1038/bjc.2014.210.
750 41. Szolek A, Schubert B, Mohr C, Sturm M, Feldhahn M, Kohlbacher O. OptiType:
751 precision HLA typing from next-generation sequencing data. Bioinformatics
752 **2014**;30(23):3310-6 doi 10.1093/bioinformatics/btu548.
753 42. Hundal J, Carreno BM, Petti AA, Linette GP, Griffith OL, Mardis ER*, et al.* pVAC-Seq:
754 A genome-guided in silico approach to identifying tumor neoantigens. Genome Med
755 **2016**;8(1):11 doi 10.1186/s13073-016-0264-5.
756 43. Li B, Severson E, Pignon JC, Zhao H, Li T, Novak J*, et al.* Comprehensive analyses
757 of tumor immunity: implications for cancer immunotherapy. Genome Biol
758 **2016**;17(1):174 doi 10.1186/s13059-016-1028-7.
759 44. Li B, Li T, Wang B, Dou R, Zhang J, Liu JS*, et al.* Ultrasensitive detection of TCR
760 hypervariable-region sequences in solid-tissue RNA-seq data. Nat Genet
761 **2017**;49(4):482-3 doi 10.1038/ng.3820.
762 45. Hu X, Zhang J, Wang J, Fu J, Li T, Zheng X*, et al.* Landscape of B cell immunity and
763 related immune evasion in human cancers. Nat Genet **2019**;51(3):560-7 doi
764 10.1038/s41588-018-0339-x.
765 46. Ivetic A, Hoskins Green HL, Hart SJ. L-selectin: A Major Regulator of Leukocyte
766 Adhesion, Migration and Signaling. Front Immunol **2019**;10:1068 doi
767 10.3389/fimmu.2019.01068.
768 47. Gorabi AM, Hajighasemi S, Kiaie N, Gheibi Hayat SM, Jamialahmadi T, Johnston TP*,*
769 *et al.* The pivotal role of CD69 in autoimmunity. J Autoimmun **2020**;111:102453 doi
770 10.1016/j.jaut.2020.102453.
771 48. Greenwald RJ, Freeman GJ, Sharpe AH. The B7 family revisited. Annu Rev Immunol
772 **2005**;23:515-48 doi 10.1146/annurev.immunol.23.021704.115611.
773 49. Grewal IS, Flavell RA. The CD40 ligand. At the center of the immune universe?
774 Immunol Res **1997**;16(1):59-70 doi 10.1007/BF02786323.
775 50. Thomas N, Best K, Cinelli M, Reich-Zeliger S, Gal H, Shifrut E*, et al.* Tracking global
776 changes induced in the CD4 T-cell receptor repertoire by immunization with a complex
777 antigen using short stretches of CDR3 protein sequence. Bioinformatics
778 **2014**;30(22):3181-8 doi 10.1093/bioinformatics/btu523.
779 51. Shugay M, Bagaev DV, Turchaninova MA, Bolotin DA, Britanova OV, Putintseva EV*,*
780 *et al.* VDJtools: Unifying Post-analysis of T Cell Receptor Repertoires. PLoS Comput
781 Biol **2015**;11(11):e1004503 doi 10.1371/journal.pcbi.1004503.
782 52. Cai H, Degliangeli F, Palitzsch B, Gerlitzki B, Kunz H, Schmitt E*, et al.* Glycopeptide-
783 functionalized gold nanoparticles for antibody induction against the tumor associated
784 mucin-1 glycoprotein. Bioorg Med Chem **2016**;24(5):1132-5 doi
785 10.1016/j.bmc.2016.01.044.
786 53. Cai H, Chen MS, Sun ZY, Zhao YF, Kunz H, Li YM. Self-adjuvanting synthetic
787 antitumor vaccines from MUC1 glycopeptides conjugated to T-cell epitopes from
788 tetanus toxoid. Angew Chem Int Ed Engl **2013**;52(23):6106-10 doi
789 10.1002/anie.201300390.
790 54. Schoenberger SP, Toes RE, van der Voort EI, Offringa R, Melief CJ. T-cell help for
791 cytotoxic T lymphocytes is mediated by CD40-CD40L interactions. Nature
792 **1998**;393(6684):480-3 doi 10.1038/31002.

793 55. Ginaldi L, De Martinis M, Matutes E, Farahat N, Morilla R, Catovsky D. Levels of
794 expression of CD19 and CD20 in chronic B cell leukaemias. J Clin Pathol
795 **1998**;51(5):364-9 doi 10.1136/jcp.51.5.364.
796 56. Wang K, Wei G, Liu D. CD19: a biomarker for B cell development, lymphoma diagnosis
797 and therapy. Exp Hematol Oncol **2012**;1(1):36 doi 10.1186/2162-3619-1-36.
798 57. Havenar-Daughton C, Lindqvist M, Heit A, Wu JE, Reiss SM, Kendric K*, et al.* CXCL13
799 is a plasma biomarker of germinal center activity. Proc Natl Acad Sci U S A
800 **2016**;113(10):2702-7 doi 10.1073/pnas.1520112113.
801 58. Kobayashi D, Endo M, Ochi H, Hojo H, Miyasaka M, Hayasaka H. Regulation of CCR7-
802 dependent cell migration through CCR7 homodimer formation. Sci Rep
803 **2017**;7(1):8536 doi 10.1038/s41598-017-09113-4.
804 59. Coppola D, Nebozhyn M, Khalil F, Dai H, Yeatman T, Loboda A*, et al.* Unique ectopic
805 lymph node-like structures present in human primary colorectal carcinoma are
806 identified by immune gene array profiling. Am J Pathol **2011**;179(1):37-45 doi
807 10.1016/j.ajpath.2011.03.007.
808 60. Messina JL, Fenstermacher DA, Eschrich S, Qu X, Berglund AE, Lloyd MC*, et al.* 12-
809 Chemokine gene signature identifies lymph node-like structures in melanoma:
810 potential for patient selection for immunotherapy? Sci Rep **2012**;2:765 doi
811 10.1038/srep00765.
812 61. Lambrechts D, Wauters E, Boeckx B, Aibar S, Nittner D, Burton O*, et al.* Phenotype
813 molding of stromal cells in the lung tumor microenvironment. Nat Med
814 **2018**;24(8):1277-89 doi 10.1038/s41591-018-0096-5.
815 62. Wu TD, Madireddi S, de Almeida PE, Banchereau R, Chen YJ, Chitre AS*, et al.*
816 Peripheral T cell expansion predicts tumour infiltration and clinical response. Nature
817 **2020**;579(7798):274-8 doi 10.1038/s41586-020-2056-8.
818 63. Efremova M, Vento-Tormo M, Teichmann SA, Vento-Tormo R. CellPhoneDB: inferring
819 cell-cell communication from combined expression of multi-subunit ligand-receptor
820 complexes. Nat Protoc **2020**;15(4):1484-506 doi 10.1038/s41596-020-0292-x.
821 64. Cassetta L, Pollard JW. Targeting macrophages: therapeutic approaches in cancer.
822 Nat Rev Drug Discov **2018**;17(12):887-904 doi 10.1038/nrd.2018.169.
823 65. Xu B, Wang S, Zhou M, Huang Y, Fu R, Guo C*, et al.* The ratio of circulating follicular
824 T helper cell to follicular T regulatory cell is correlated with disease activity in systemic
825 lupus erythematosus. Clin Immunol **2017**;183:46-53 doi 10.1016/j.clim.2017.07.004.
826 66. Tuccillo FM, de Laurentiis A, Palmieri C, Fiume G, Bonelli P, Borrelli A*, et al.* Aberrant
827 glycosylation as biomarker for cancer: focus on CD43. Biomed Res Int
828 **2014**;2014:742831 doi 10.1155/2014/742831.
829 67. Kufe DW. Mucins in cancer: function, prognosis and therapy. Nat Rev Cancer
830 **2009**;9(12):874-85 doi 10.1038/nrc2761.
831 68. Hollingsworth MA, Swanson BJ. Mucins in cancer: protection and control of the cell
832 surface. Nat Rev Cancer **2004**;4(1):45-60 doi 10.1038/nrc1251.
833 69. van Kooten C, Banchereau J. CD40-CD40 ligand. J Leukoc Biol **2000**;67(1):2-17 doi
834 10.1002/jlb.67.1.2.
835 70. Nerviani A, Pitzalis C. Role of chemokines in ectopic lymphoid structures formation in
836 autoimmunity and cancer. J Leukoc Biol **2018**;104(2):333-41 doi
837 10.1002/JLB.3MR0218-062R.
838 71. Domeier PP, Schell SL, Rahman ZS. Spontaneous germinal centers and autoimmunity.
839 Autoimmunity **2017**;50(1):4-18 doi 10.1080/08916934.2017.1280671.
840 72. Sage PT, Sharpe AH. T follicular regulatory cells in the regulation of B cell responses.
841 Trends Immunol **2015**;36(7):410-8 doi 10.1016/j.it.2015.05.005.
842 73. Sage PT, Ron-Harel N, Juneja VR, Sen DR, Maleri S, Sungnak W*, et al.* Suppression
843 by TFR cells leads to durable and selective inhibition of B cell effector function. Nat
844 Immunol **2016**;17(12):1436-46 doi 10.1038/ni.3578.
845 74. Wing JB, Tekguc M, Sakaguchi S. Control of Germinal Center Responses by T-
846 Follicular Regulatory Cells. Front Immunol **2018**;9:1910 doi
847 10.3389/fimmu.2018.01910.

75. Viguier M, Lemaitre F, Verola O, Cho MS, Gorochov G, Dubertret L*, et al.* Foxp3 expressing CD4+CD25(high) regulatory T cells are overrepresented in human metastatic melanoma lymph nodes and inhibit the function of infiltrating T cells. J Immunol **2004**;173(2):1444-53 doi 10.4049/jimmunol.173.2.1444.
76. Clement RL, Daccache J, Mohammed MT, Diallo A, Blazar BR, Kuchroo VK*, et al.* Follicular regulatory T cells control humoral and allergic immunity by restraining early B cell responses. Nat Immunol **2019**;20(10):1360-71 doi 10.1038/s41590-019-0472-4.
77. Finkin S, Yuan D, Stein I, Taniguchi K, Weber A, Unger K*, et al.* Ectopic lymphoid structures function as microniches for tumor progenitor cells in hepatocellular carcinoma. Nat Immunol **2015**;16(12):1235-44 doi 10.1038/ni.3290.
78. Di Caro G, Bergomas F, Grizzi F, Doni A, Bianchi P, Malesci A*, et al.* Occurrence of tertiary lymphoid tissue is associated with T-cell infiltration and predicts better prognosis in early-stage colorectal cancers. Clin Cancer Res **2014**;20(8):2147-58 doi 10.1158/1078-0432.CCR-13-2590.
79. Gu-Trantien C, Loi S, Garaud S, Equeter C, Libin M, de Wind A*, et al.* CD4(+) follicular helper T cell infiltration predicts breast cancer survival. J Clin Invest **2013**;123(7):2873-92 doi 10.1172/JCI67428.
80. Dieu-Nosjean MC, Antoine M, Danel C, Heudes D, Wislez M, Poulot V*, et al.* Long-term survival for patients with non-small-cell lung cancer with intratumoral lymphoid structures. J Clin Oncol **2008**;26(27):4410-7 doi 10.1200/JCO.2007.15.0284.
81. Remark R, Lupo A, Alifano M, Biton J, Ouakrim H, Stefani A*, et al.* Immune contexture and histological response after neoadjuvant chemotherapy predict clinical outcome of lung cancer patients. Oncoimmunology **2016**;5(12):e1255394 doi 10.1080/2162402X.2016.1255394.
82. Germain C, Gnjatic S, Tamzalit F, Knockaert S, Remark R, Goc J*, et al.* Presence of B cells in tertiary lymphoid structures is associated with a protective immunity in patients with lung cancer. Am J Respir Crit Care Med **2014**;189(7):832-44 doi 10.1164/rccm.201309-1611OC.
83. Dejima H, Hu X, Chen R, Zhang J, Junya F, Parra EC*, et al.* Immune evolution from preneoplasia to invasive lung adenocarcinomas and underlying molecular features. **2020**:2020.07.11.20142992 doi 10.1101/2020.07.11.20142992 %J medRxiv.
84. McLaren W, Gil L, Hunt SE, Riat HS, Ritchie GR, Thormann A*, et al.* The Ensembl Variant Effect Predictor. Genome Biol **2016**;17(1):122 doi 10.1186/s13059-016-0974-4.
85. Mayakonda A, Lin DC, Assenov Y, Plass C, Koeffler HP. Maftools: efficient and comprehensive analysis of somatic variants in cancer. Genome Res **2018**;28(11):1747-56 doi 10.1101/gr.239244.118.
86. Gu Z, Eils R, Schlesner M. Complex heatmaps reveal patterns and correlations in multidimensional genomic data. Bioinformatics **2016**;32(18):2847-9 doi 10.1093/bioinformatics/btw313.
87. Aran D, Hu Z, Butte AJ. xCell: digitally portraying the tissue cellular heterogeneity landscape. Genome Biol **2017**;18(1):220 doi 10.1186/s13059-017-1349-1.
88. Sims JS, Grinshpun B, Feng Y, Ung TH, Neira JA, Samanamud JL*, et al.* Diversity and divergence of the glioma-infiltrating T-cell receptor repertoire. Proc Natl Acad Sci U S A **2016**;113(25):E3529-37 doi 10.1073/pnas.1601012113.
89. Kitaura K, Yamashita H, Ayabe H, Shini T, Matsutani T, Suzuki R. Different Somatic Hypermutation Levels among Antibody Subclasses Disclosed by a New Next-Generation Sequencing-Based Antibody Repertoire Analysis. Front Immunol **2017**;8:389 doi 10.3389/fimmu.2017.00389.
90. Looney TJ, Lee JY, Roskin KM, Hoh RA, King J, Glanville J*, et al.* Human B-cell isotype switching origins of IgE. J Allergy Clin Immunol **2016**;137(2):579-86 e7 doi 10.1016/j.jaci.2015.07.014.
91. Racle J, de Jonge K, Baumgaertner P, Speiser DE, Gfeller D. Simultaneous enumeration of cancer and immune cell types from bulk tumor gene expression data. Elife **2017**;6 doi 10.7554/eLife.26476.

903 92. Wang CS, Dongqing. MAESTRO: Model-based AnalysEs of Single-cell Transcriptome
904 and Regulome. **2020** doi 10.5281/zenodo.3862813.
905
906

907 # FIGURE LEGEND

908

909 **Figure 1. MIA tumors are characterized by highly mutated and over-expressed mucins,**
910 **cytokine::cytokine-receptor interactions, and EGFR mutations**

911 **(A)** Representative HE images of MIA. Top at 4X magnification, scale bar 300 μm. Boxed area
912 of top image shown below (20x magnification, scale bar 50 μm). Lymphocyte infiltration
913 (dashed box, bottom) and MIA tumor cells (solid box, bottom) are shown. **(B)** Normalized
914 enrichment scores (x-axis) of tumor-upregulated KEGG pathways. Colors indicate different
915 KEGG pathway categories. Asterisks denote significance level (*** FDR < 0.001; ** FDR <
916 0.01; * FDR < 0.05; NS FDR > 0.05). **(C)** Alterations of mucin genes in MIA patients. Each bar
917 represents a MIA patient. Shown are mutation classifications, and expression status. Values
918 on the right indicate the proportion of patients in which the gene was either mutated or had
919 altered expression. **(D)** Most commonly mutated genes in MIA patients. Colors indicate variant
920 type. Shown are the proportion of tumors containing a mutation in the indicated gene (left);
921 total number of mutations in the indicated gene (right). **(E)** Schematic of the EGFR gene,
922 showing mutations (stick and ball markers) and protein domains (color blocks).

923

924 **Figure 2. Higher B and CD4+ T cell infiltration and activation but lower CD8+ T cell**
925 **infiltration characterize MIA tumors**

926 **(A)** Comparison of immune components between tumor (red) and adjacent normal tissue (blue)
927 in MIA. Immune Cell Abundance values (y-axis) were generated from TIMER. Significance
928 levels are indicated (*** P < 0.001; ** P < 0.01; * P < 0.05; ns P> 0.05). **(B)** Immune infiltration
929 among TCGA lung adenocarcinoma (LUAD) samples separated by clinical stage (colors).
930 Comparison of fraction of TCR reads **(C)** and fraction of BCR reads (**D**) between MIA tumor
931 and adjacent normal tissues. (**E**) Comparison of gene expressions on CD4+ T cell activation
932 markers (CD69, CD40LG, IL2RA, and CD62) between MIA tumor and adjacent normal tissues.
933 Comparison of the number of BCR clusters (**F**), BCR clonotypes per kilo reads **(G)**, BCR
934 clonality **(H), and** somatic hyper-mutation rate of BCR **(I)** between MIA tumor and adjacent
935 normal tissues. Asterisks denote significance on difference between MIA tumors and adjacent
936 normal tissues (*** P < 0.001; ** P < 0.01; * P < 0.05).

937

938 **Figure 3.** ***Tumor-infiltrating B cells and T cells are activated by tumor antigens in MIA***

939 **(A)** Normalized BCR clonotype frequency on patient level. Each dot represents a BCR
940 clonotype and the normalized clonotype abundance in tumor and adjacent normal tissue. The
941 three percentage values correspond to the overall percentage of tumor-specific clonotypes
942 (58.6% in BCR), normal-specific clonotypes (38.6% in BCR), and shared (2.86% in BCR)

943 clonotypes. **(B)** Normalized TCR clonotype frequency on patient level. **(C)** Jaccard similarity
944 of the BCR/TCR clonotypes between tumor and adjacent normal tissues. Shown are shared
945 clonotypes within each patient (dark brown for BCR, dark green for TCR) and average shared
946 clonotypes between tumors and unmatched normal samples (light brown for BCR, light green
947 for TCR). **(D)** Jaccard similarity of BCR and TCR repertoire among tumors (solid line) and
948 normal tissues (dashed line) shown in top (BCR) and bottom (TCR) panel, respectively. **(E)**
949 Jaccard similarity in groups with high (blue) and low (red) mutation load (*** $P < 0.001$; ** $P <$
950 0.01; * $P < 0.05$).
951
952 **Figure 4. Mucin mutation and overexpression is associated with CD4+ T cell-mediated**
953 **B cell activation in MIA tumors**
954 **(A)** The correlation between mucins and MHCII expression. **(B)** The correlation between
955 CD40 and CD40LG expression. **(C)** The correlation between mucins and averaged level of
956 CD40 and CD40LG. **(D)** The correlation between mucin expression with IgG (green) and IgA
957 (brown) expression in MIA patients. **(E)** MIA tumors (x-axis) ranked by immune-related
958 signature score (heatmap colors). The top bar shows the average immune signature score for
959 each patient. The bottom bars show the tumor purity, expression level of mucins, MHCII
960 molecules, CD40, CD40LG, IgG, and IgA.
961
962 **Figure 5. Formation of tertiary lymphoid structure (TLS) in MIA tumors**
963 **(A)** The schema of TLS formation. The first stage is B & T cell aggregation. The second stage
964 is follicle formation with T-Zone and B-Zone. The third stage is ectopic germinal center
965 formation with formation with follicular dendritic cell in light-Zone. **(B)** Hierarchical clustering
966 of Z-score normalized gene expression of B-cell infiltration markers (CD19, CD20), follicle
967 phenotype markers (CXCR5, CXCL13), and lymphocyte homing signal markers (CCR7 and
968 CCL19). Color of the top bar represents tumor (red) or adjacent normal (blue) tissue.
969 Correlations between expression levels from these six TLS markers and immune cell
970 abundance corrected by tumor purity are shown in the right bar. **(C)** Typical observation field
971 of MIA six-plex TLS panel staining. The merged-channel multispectral image was captured
972 after 5-cycle TSA staining and DAPI counterstain, revealing a classic lymphoid structure
973 residing in MIA stromal tissue. Single channels are shown for the area bounded by the white
974 rectangle. Fake colors are assigned as DAPI: blue, CD8: yellow, CXCR5: pink, CD4: green,
975 CD20: red, CD35: cyan. Tfh cells are highlighted with white arrows (lower right corner images).
976 **(D)** Paired comparisons of CD20+ B cell density, CD4+ T cell density **(E),** CD35+ follicle
977 dendritic cell density **(F)**, and CD8+ T cell density **(G)** between Non-Follicle (Non-Fol) and TLS
978 areas.

Figure 6. Treg recruitment as potential mechanism of CD8+ T cell exclusion in tertiary lymphoid structures

(A) Comparison of immune suppressive cell infiltration estimated from XCELL between MIA tumor and adjacent normal tissues (*** $P < 0.001$; ** $P < 0.01$; * $P < 0.05$). **(B)** Plot of Tfr/Tfh marker ratio vs CD8+ T cell infiltration. FoxP3, PDCD1, and IL2RA are markers of Tfr cells, while BCL6, ICOS, IL7R are markers of Tfh cells. See text. **(C)** Typical observation field of MIA 7-plex panel staining for Tfr and Tfh. Merged multispectral image was captured after 6-cycle TSA staining and DAPI counterstain and reveals a mature TLS architecture. Single channels are shown for the area bounded by the white rectangle. Fake colors are assigned as DAPI: blue, CD8: yellow, CXCR5: pink, CD4: green, FOXP3: red, BCL6: cyan and CD3: orange. Sub-populations of CD4+ T-cells are highlighted by arrows (Tfr: red, Treg: purple, Th: green and Tfh: cyan). **(D)** Paired comparison of CD8+ T cell density between Non-Follicle (Non-Fol) and TLS areas. **(E)** Paired comparison of ratio of regulatory T cells to helper T cells between TLS and Non-Follicle areas. **(F)** Comparison of CD8+ T cell density between groups with high and low Tfr/Tfh ratio.

Figure S1. The workflow of data processing.

In this workflow, five sections were performed for analyzing transcriptome data and imaging data, including expression profiling EdgR and GSEA, mutation calling from Varscan2, estimating immune cell infiltration from TIMER and CIBERSORT, quantifying immune repertoire from TRUST3, and Morphological validation from H&E staining, multiplex IHC, multispectral imaging and spatial statistics.

Figure S2. Differential gene expression analysis.

Colors of dots represent the tumor up-regulated genes (red) and tumor down-regulated genes (blue). Top differentially expressed mucin family members, cytokines, and cytokine receptors are highlighted in Volcano plot.

Figure S3. Genetic alterations of mucin family members in TCGA LUAD.

Mutations and gene alterations in mucin family members are highlighted with different colors, including inframe mutation (pink inside), missense mutation (green inside), truncating mutation (blue inside), mRNA high expression (pink outside), mRNA low expression (blue outside), and no alterations (grey).

Figure S4. Mutation overview of MIA.

The summary of variants from MIA, including the number of different variant classifications and SNV classes for each patient (**A**) and the frequency of nucleotide changes (**B**). (**C**) Comparison of msi score between high and low CT transition. (**D**) The mutation loci in EGFR. (**E**) The mutation pattern of EGFR, KRAS and TP53 in MIA.

Figure S5. Neo-epitope prediction for top mutated genes.

(**A**) Mutation rate (dark blue bar) and neo-epitope rate (MHC-I bound, light blue bar) among 59 patients for top 15 mutate genes. (**B**) Neo-epitope binding affinity and gene expression for top 15 mutated genes in patients. Each dot represents a predicted neo-epitope in a patient. Epitopes predicted from MUC20 (green), MUC4 (yellow), and MUC6 (purple) are highlighted with text. The color of dot represents the types of gene expression changes, including up-regulation (red), down-regulation (blue) and no change (grey).

Figure S6. Immune infiltration estimation from CIBERSORT.

Comparison of Immune cell infiltration estimated from CIBERSORT ("Absolute" mode) between MIA tumor and adjacent normal tissues.

1030 **Figure S7. Immune repertoire metrics in MIA.** Comparison of faction of TCR reads (**A**),
1031 faction of BCR reads (**B**) between MIA tumor and normal tissues. (**C**) The ratio of Ig class
1032 switch recombination between IgG and IgA in MIA tumor and normal tissues. (*** P < 0.001;
1033 ** P < 0.01; * P < 0.05).
1034
1035 **Figure S8. Association between molecules mediated B-CD4+ T activation and immune-**
1036 **related signature score.**
1037 Association between MHCII level (**A**), mucin level (**B**), CD40 level (**C**), CD40LG level (**D**), IgG
1038 level (**E**), IgA level (**F**), and percentage of tumor unique BCR clonotypes (**G**) with immune-
1039 related signature score. MIA tumors are divided into “immune-low” and “immune-high” groups
1040 based on the median immune-related signature score. (*** P < 0.001; ** P < 0.01; * P < 0.05).
1041
1042 **Figure S9. 6 TLS markers and a 12-chemokine signature for predicting TLS existence.**
1043 (**A**) Association between 6 TLS markers expression and a 12-chemokine signature score. (**B**)
1044 Association between 6 TLS markers expression and immune-related signature score. (**C**)
1045 Association between a 12-chemokine signature score and immune-related signature score.
1046 MIA tumors are divided into “immune-low” and “immune-high” groups based on the median
1047 immune-related signature score. (*** P < 0.001; ** P < 0.01; * P < 0.05).
1048
1049 **Figure S10. B, follicular T helper, and follicular T regulatory cells are enriched in NSCLC**
1050 **tumors in an independent single-cell RNA-seq dataset NSCLC_GSE139555.** (**A**) (left) cell
1051 distribution in different tissues and each color represents a type of tissue (left), including blood,
1052 NAT (normal adjacent tissue), and tumor;(right) cell type annotation and each color represents
1053 a cell type. (**B**) Gene expressions for CD4, CXCR5, FOXP3, and MS4A1 are compared
1054 between tumor and NAT across different cell types. (*** P < 0.001; ** P < 0.01; * P < 0.05).
1055
1056 **Figure S11. B, follicular T helper, and follicular T regulatory cells are enriched in NSCLC**
1057 **tumors in an independent single-cell RNA-seq dataset NSCLC_EMTAB6149.** (**A**) cell type
1058 annotations. Each color represents a cell type. (**B**) Cluster averaged signature expression
1059 comparison between tumor (red) and normal tissues (blue) of different cell types. (**C**)
1060 Receptor-ligand pairs enrichment of different cell-cell interactions. The dot color represents
1061 the expression level of the receptor-ligand pairs and the dot size represents the enrichment
1062 significance of interaction pairs.
1063
1064 **Figure S12. Evidence of TLS presence from H&E staining.** The red circles denote the
1065 inferred TLS B and T cell aggregation.
1066

Figure S13. Different maturation level of TLS formation and corresponding CD8+ T cell infiltration. TLS formation stained by CD4(green), CD20(red), and CD35(cyan) co-localization in the left panel and CD8+ T cell infiltration in the right panel from the same observation field are shown.

Figure S14. Normal germinal center in tonsil and ectopic germinal center in MIA. Normal germinal center in tonsil (**A**) and ectopic germinal center in MIA (**B**). T-cell zone, B-cell zone, dark zone, and light zone consist of GC in tonsil or EGC in MIA stained by immunofluorescence (left) and immunohistochemistry (right).

Figure S15. Multispectral analysis for segmenting tissues, cells and phenotypes. Segmentation for six-plex panel for TLS (**A**) and seven-plex panel for Tfr and Tfh (**B**). Each observation field could be segmented into 5 tissue categories as adenocarcinoma tissue (ACT), Non-Follicle area (Non-Fol), TLS T-cell area (TLS-T), TLS B-cell area (TLS-B) and light zone of germinal center (EGC-LZ) in both six-plex panel (top) and seven-plex panel (bottom). Five phenotypes were contained in six-plex panel, including CC (blue), CD8+ T (yellow), CD4+ T (green), CD20+ B (red), and CD35+ FDC (cyan). Seven phenotypes were contained in seven-plex, including CC (blue), CTL (yellow), Th (green), Tfh (cyan), Treg (pink), Tfr (red), and oLeu (black). ACC: Adenocarcinoma cancer cell; CC: cancer cell; Non-Fol: Non-follicular area; CTL: cytotoxic T lymphocyte; Th: T helper; Tfh: follicular T helper; Treg: regulatory T-cell; Tfr: follicular Treg; FDC: follicular dendritic cell; oLeu: other leukocyte.

Figure S16. Down-regulated PD-L1 in MIA tumors. Comparison of the expression of PD-L1 (CD274) in tumor (red) and adjacent-normal (blue) samples (*** $P < 0.001$; ** $P < 0.01$; * $P < 0.05$).

Figure S17. The ratio of regulatory T to helper T and CD8+ T cell infiltration in Non-follicle areas. CD8+ T cell comparison between groups with high (red) and low (blue) ratio of regulatory T to helper T.

Figure1

A

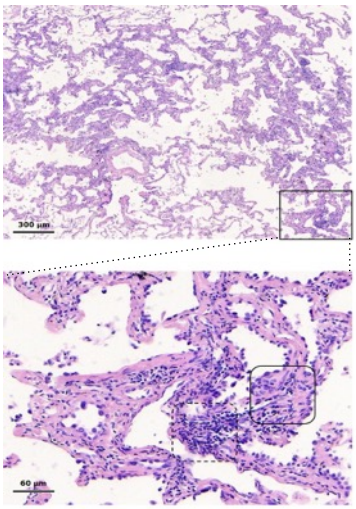

B

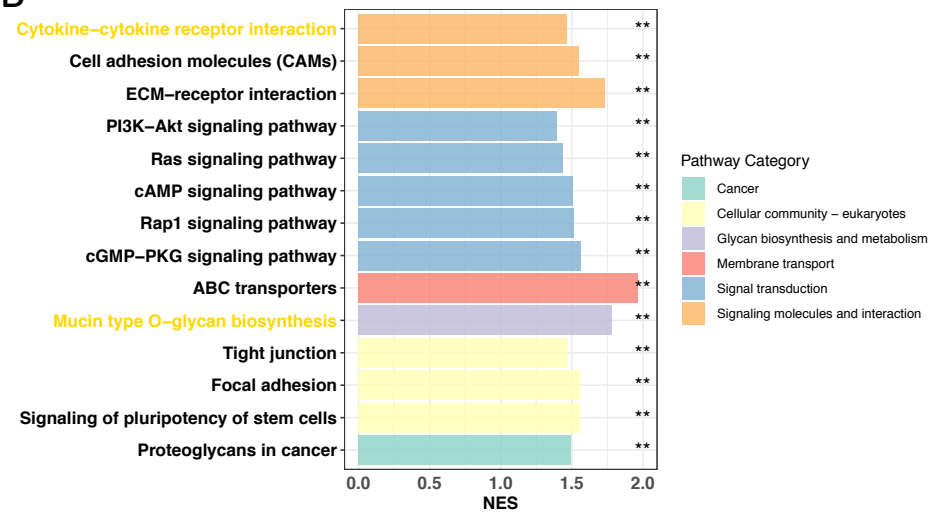

C

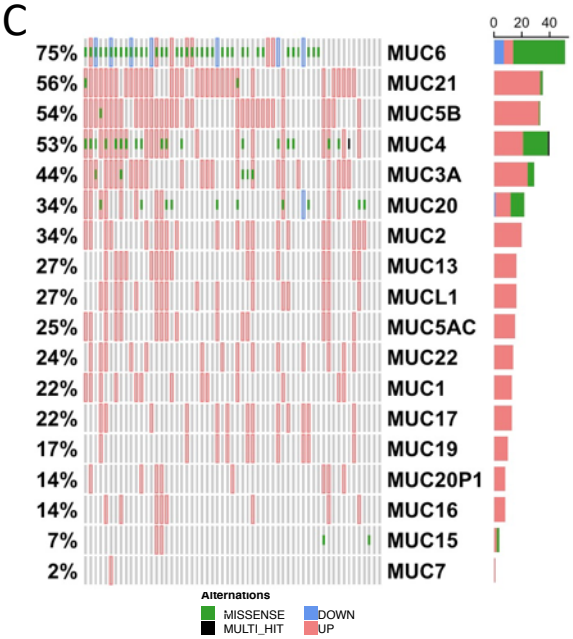

D

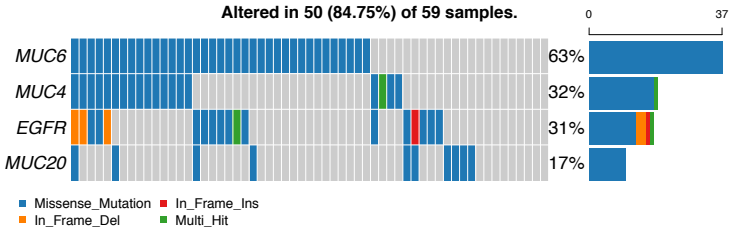

E

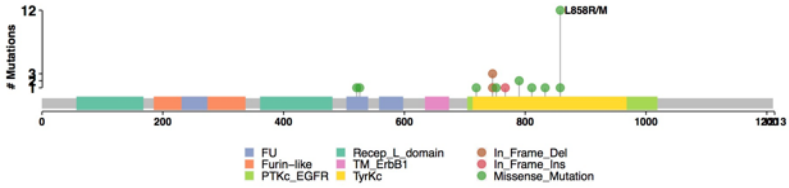

Figure 2

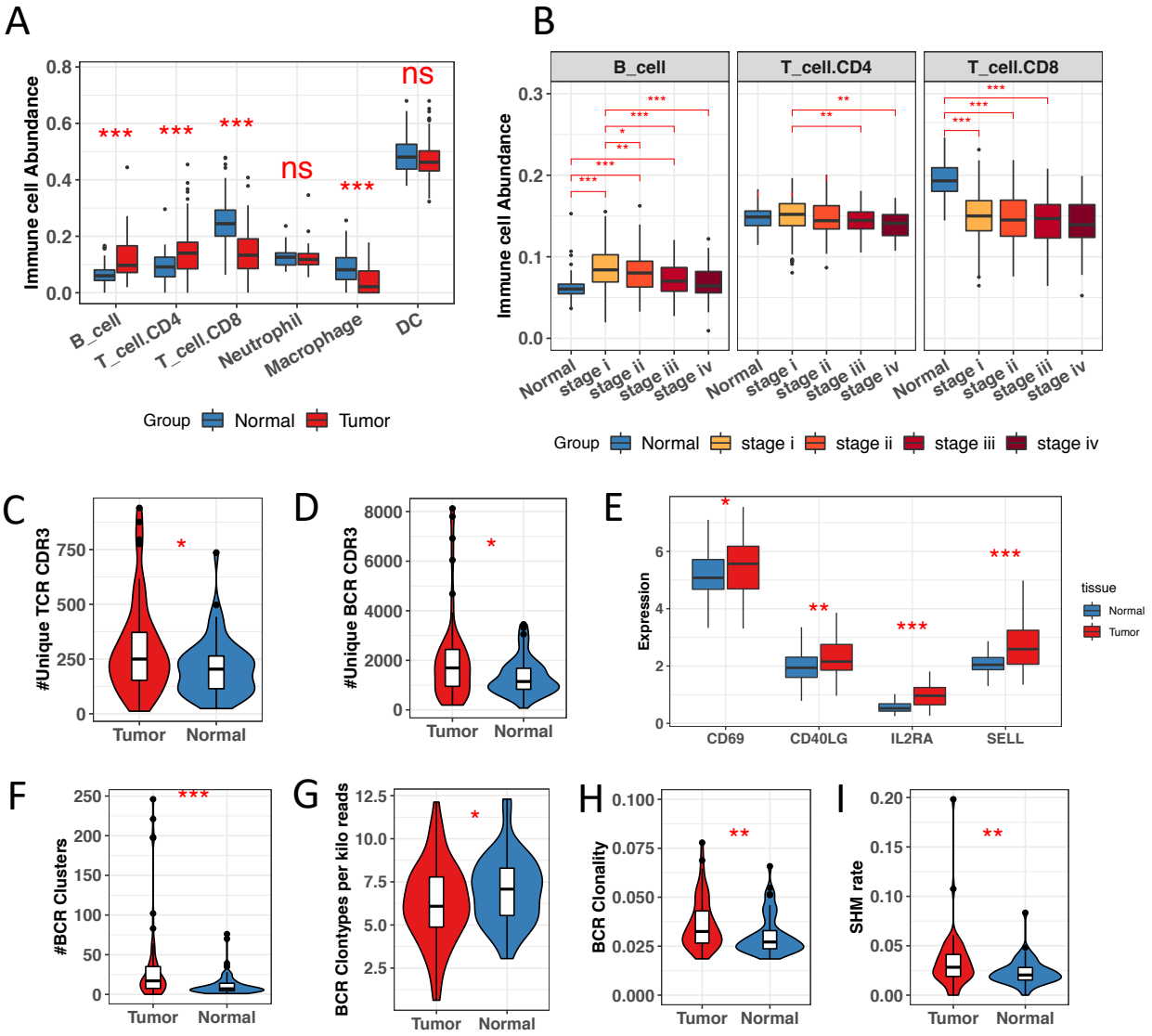
A
Immune cell Abundance
0.8
0.6
0.4
0.2
0.0
***
***
***
ns
***
ns
B_cell
T_cell.CD4
T_cell.CD8
Neutrophil
Macrophage
DC
Group
Normal
Tumor
B
B_cell
T_cell.CD4
T_cell.CD8
Immune cell Abundance
0.3
0.2
0.1
0.0
Normal
stage i
stage ii
stage iii
stage iv
Group
Normal
stage i
stage ii
stage iii
stage iv
C
#Unique TCR CDR3
750
500
250
0
*
Tumor
Normal
D
#Unique BCR CDR3
8000
6000
4000
2000
0
*
Tumor
Normal
E
Expression
6
4
2
0
*
**
***
***
CD69
CD40LG
IL2RA
SELL
tissue
Normal
Tumor
F
#BCR Clusters
250
200
150
100
50
0
***
Tumor
Normal
G
BCR Clontypes per kilo reads
12.5
10.0
7.5
5.0
2.5
*
Tumor
Normal
H
BCR Clonality
0.100
0.075
0.050
0.025
0.000
**
Tumor
Normal
I
SHM rate
0.20
0.15
0.10
0.05
0.00
**
Tumor
Normal

Figure 3

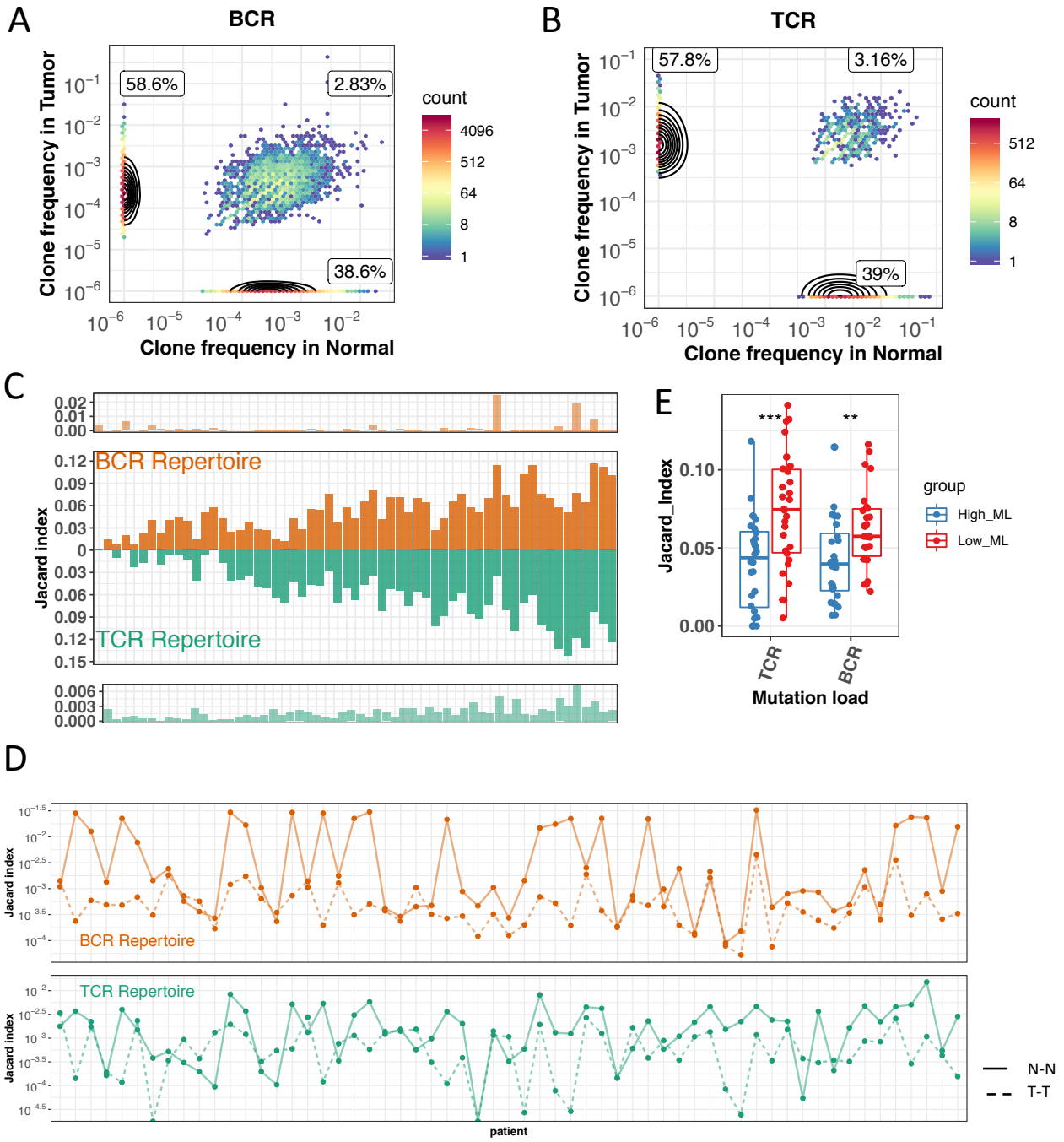
A
BCR
58.6%
2.83%
38.6%
Clone frequency in Tumor
Clone frequency in Normal
count
4096
512
64
8
1
B
TCR
57.8%
3.16%
39%
Clone frequency in Tumor
Clone frequency in Normal
count
512
64
8
1
C
BCR Repertoire
TCR Repertoire
Jacard index
D
BCR Repertoire
TCR Repertoire
Jacard index
patient
N-N
T-T
E
Jacard_Index
Mutation load
TCR
BCR
***
**
group
High_ML
Low_ML

Figure 4

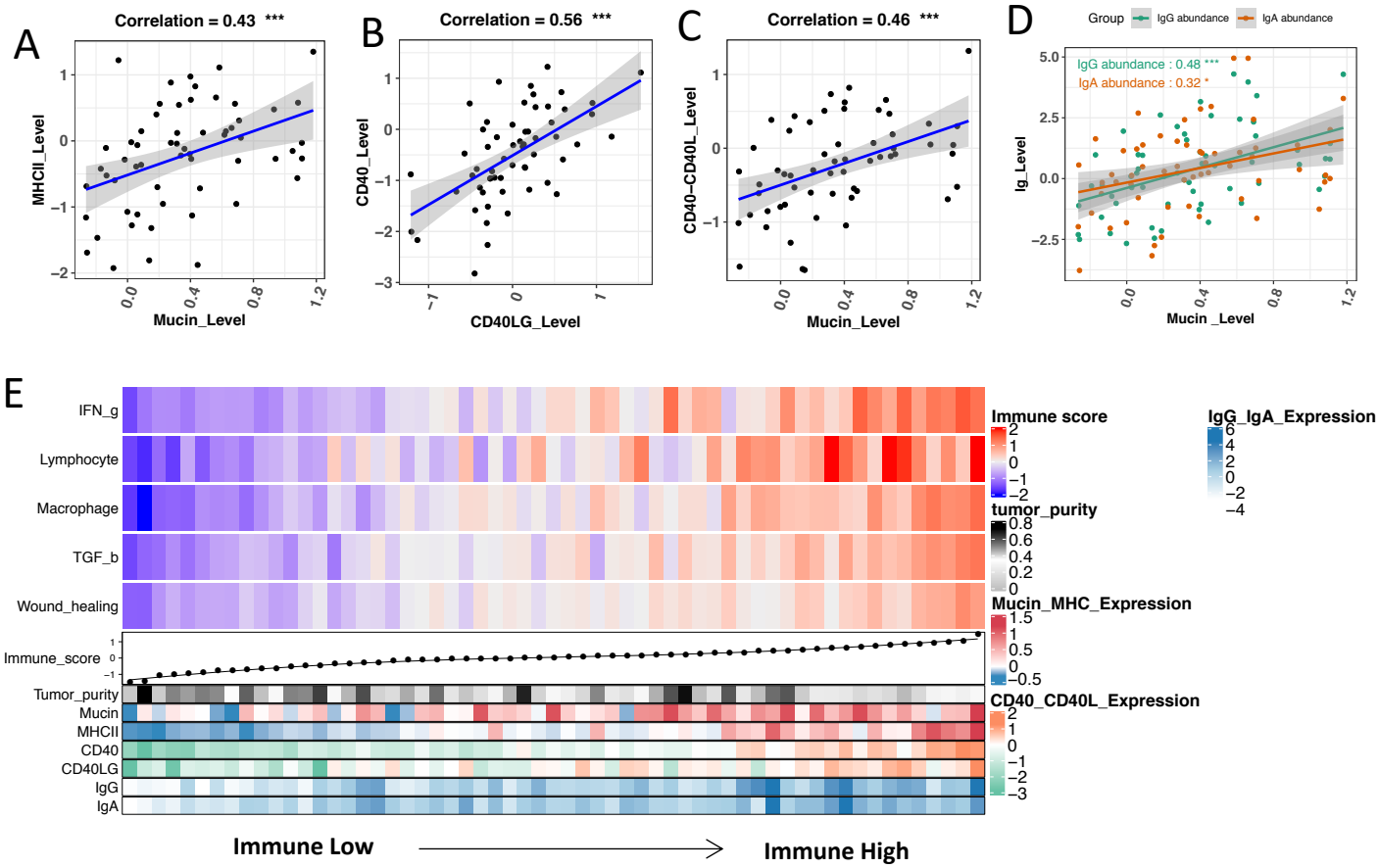
A
Correlation = 0.43 ***
MHCII_Level
Mucin_Level
B
Correlation = 0.56 ***
CD40_Level
CD40LG_Level
C
Correlation = 0.46 ***
CD40−CD40L_Level
Mucin_Level
D
Group
IgG abundance
IgA abundance
IgG abundance : 0.48 ***
IgA abundance : 0.32 *
Ig_Level
Mucin _Level
E
IFN_g
Lymphocyte
Macrophage
TGF_b
Wound_healing
Immune_score
Tumor_purity
Mucin
MHCII
CD40
CD40LG
IgG
IgA
Immune score
tumor_purity
Mucin_MHC_Expression
CD40_CD40L_Expression
IgG_IgA_Expression
Immune Low
Immune High

Figure 5

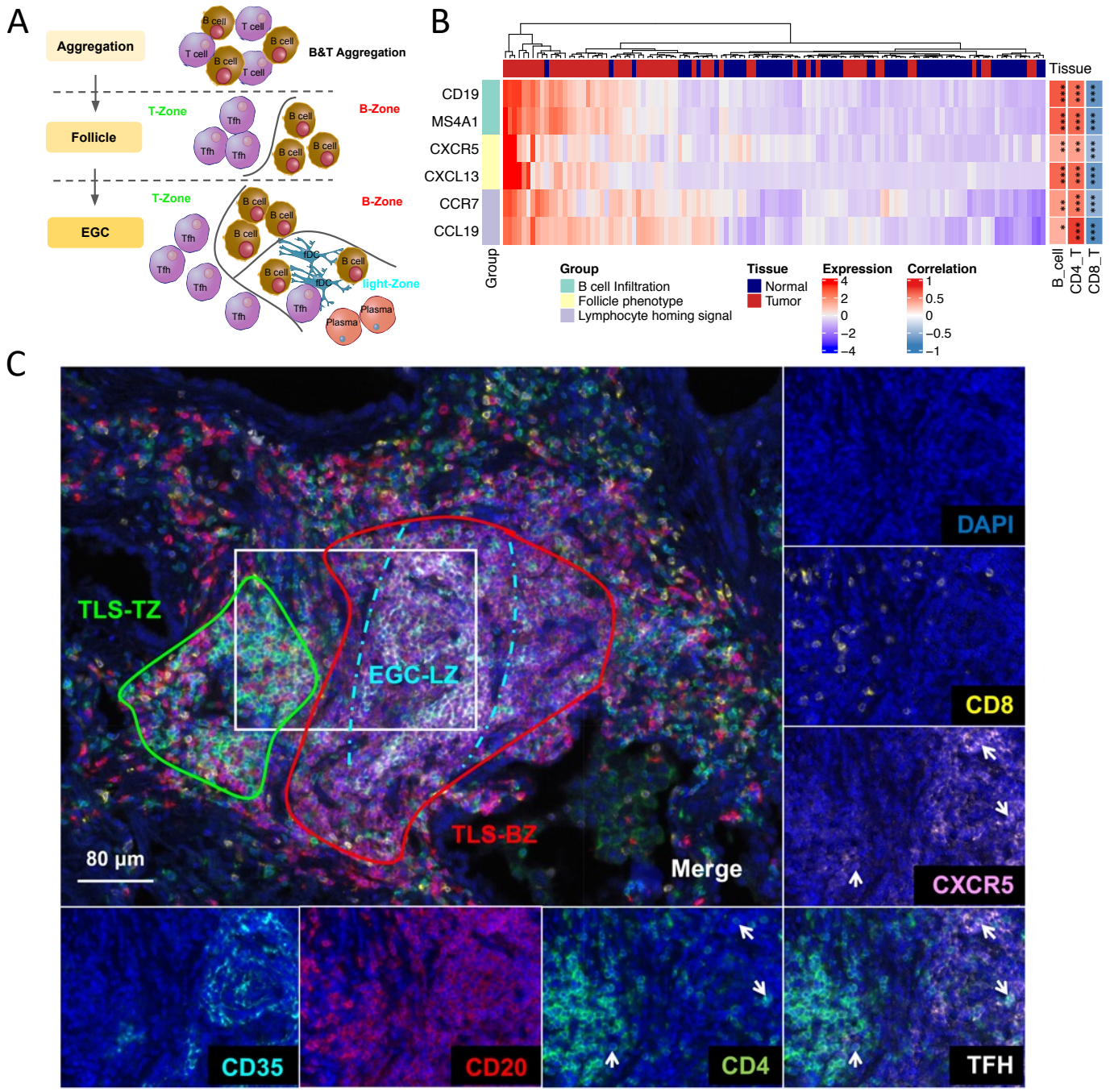
A
Aggregation
B&T Aggregation
T-Zone
B-Zone
Follicle
EGC
light-Zone
B cell
T cell
Tfh
fDC
Plasma
B
Tissue
CD19
MS4A1
CXCR5
CXCL13
CCR7
CCL19
Group
B_cell
CD4_T
CD8_T
Group
B cell Infiltration
Follicle phenotype
Lymphocyte homing signal
Tissue
Normal
Tumor
Expression
Correlation
C
TLS-TZ
EGC-LZ
TLS-BZ
80 μm
Merge
DAPI
CD8
CXCR5
CD35
CD20
CD4
TFH
D
p < 0.0001
CD20+ B density
Non-Fol
TLS
E
p < 0.0001
CD4+ T density
F
p < 0.0001
CD35+ FDC density
G
p < 0.0001
CD8+ T density

Figure 6

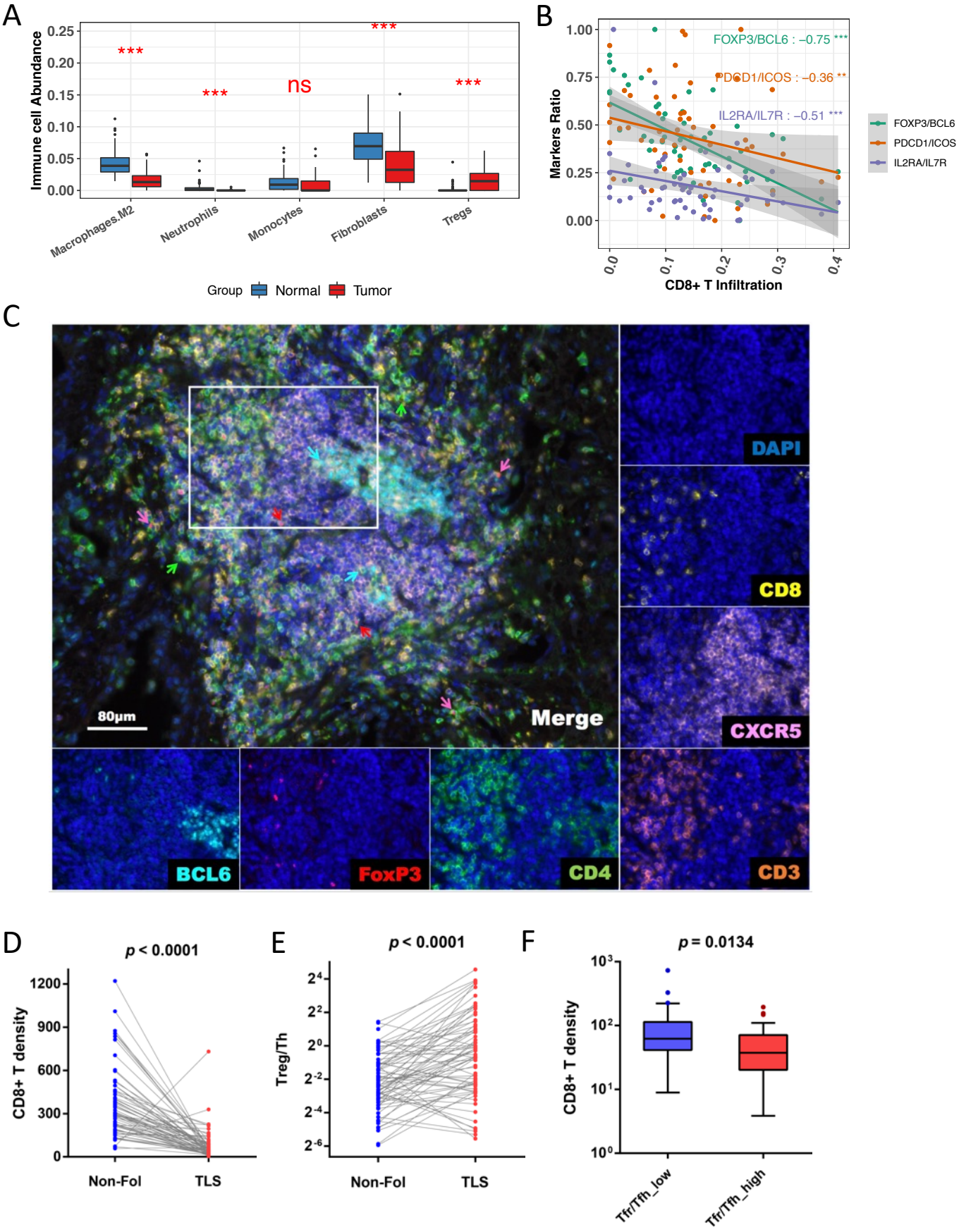
A
Immune cell Abundance
0.25
0.20
0.15
0.10
0.05
0.00
***
***
ns
***
***
Macrophages.M2
Neutrophils
Monocytes
Fibroblasts
Tregs
Group
Normal
Tumor
B
Markers Ratio
1.00
0.75
0.50
0.25
0.00
FOXP3/BCL6 : −0.75 ***
PDCD1/ICOS : −0.36 **
IL2RA/IL7R : −0.51 ***
FOXP3/BCL6
PDCD1/ICOS
IL2RA/IL7R
0.0
0.1
0.2
0.3
0.4
CD8+ T Infiltration
C
DAPI
CD8
CXCR5
CD3
Merge
80μm
BCL6
FoxP3
CD4
D
p < 0.0001
CD8+ T density
1200
900
600
300
0
Non-Fol
TLS
E
p < 0.0001
Treg/Th
2^4
2^2
2^0
2^-2
2^-4
2^-6
Non-Fol
TLS
F
p = 0.0134
CD8+ T density
10^3
10^2
10^1
10^0
Tfr/Tfh_low
Tfr/Tfh_high

Figure S1

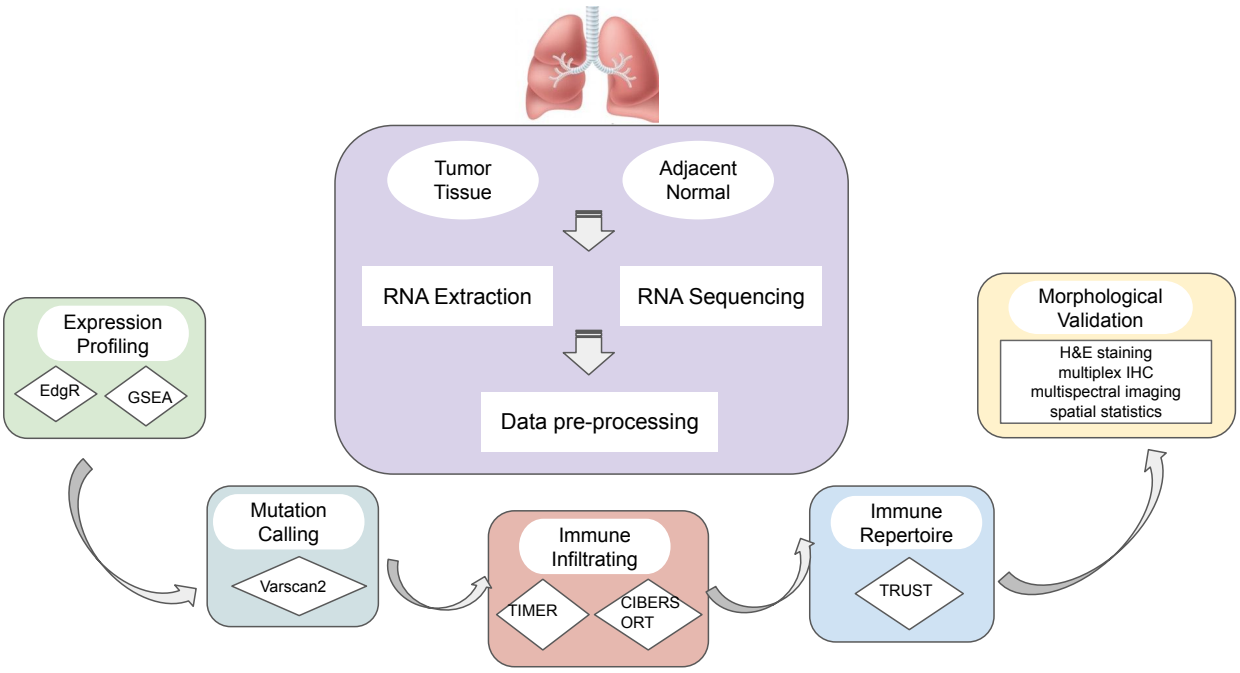
Tumor Tissue
Adjacent Normal
RNA Extraction
RNA Sequencing
Data pre-processing
Expression Profiling
EdgR
GSEA
Morphological Validation
H&E staining
multiplex IHC
multispectral imaging
spatial statistics
Mutation Calling
Varscan2
Immune Infiltrating
TIMER
CIBERSORT
Immune Repertoire
TRUST

Figure S2

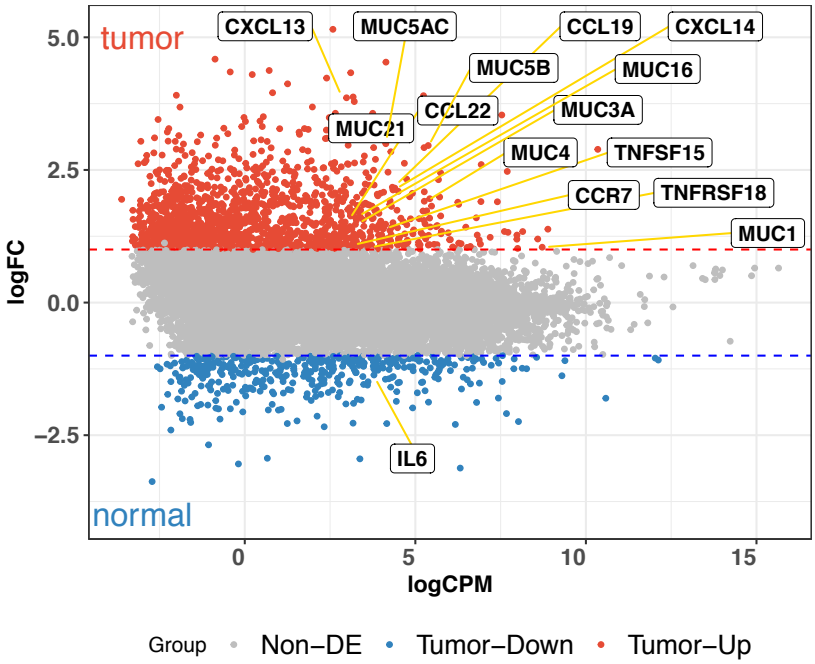
tumor
normal
CXCL13
MUC5AC
CCL19
CXCL14
MUC5B
MUC16
CCL22
MUC3A
MUC21
MUC4
TNFSF15
CCR7
TNFRSF18
MUC1
IL6
5.0
2.5
0.0
−2.5
logFC
0
5
10
15
logCPM
Group
Non−DE
Tumor−Down
Tumor−Up

Figure S3

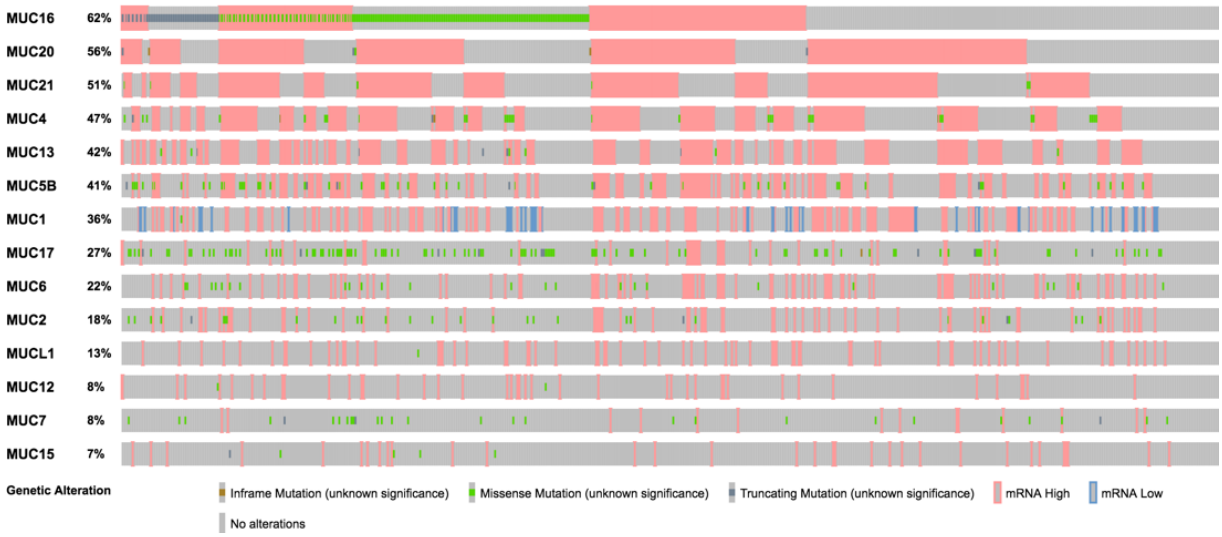
MUC16 62%
MUC20 56%
MUC21 51%
MUC4 47%
MUC13 42%
MUC5B 41%
MUC1 36%
MUC17 27%
MUC6 22%
MUC2 18%
MUCL1 13%
MUC12 8%
MUC7 8%
MUC15 7%
Genetic Alteration
Inframe Mutation (unknown significance)
Missense Mutation (unknown significance)
Truncating Mutation (unknown significance)
mRNA High
mRNA Low
No alterations

Figure S4

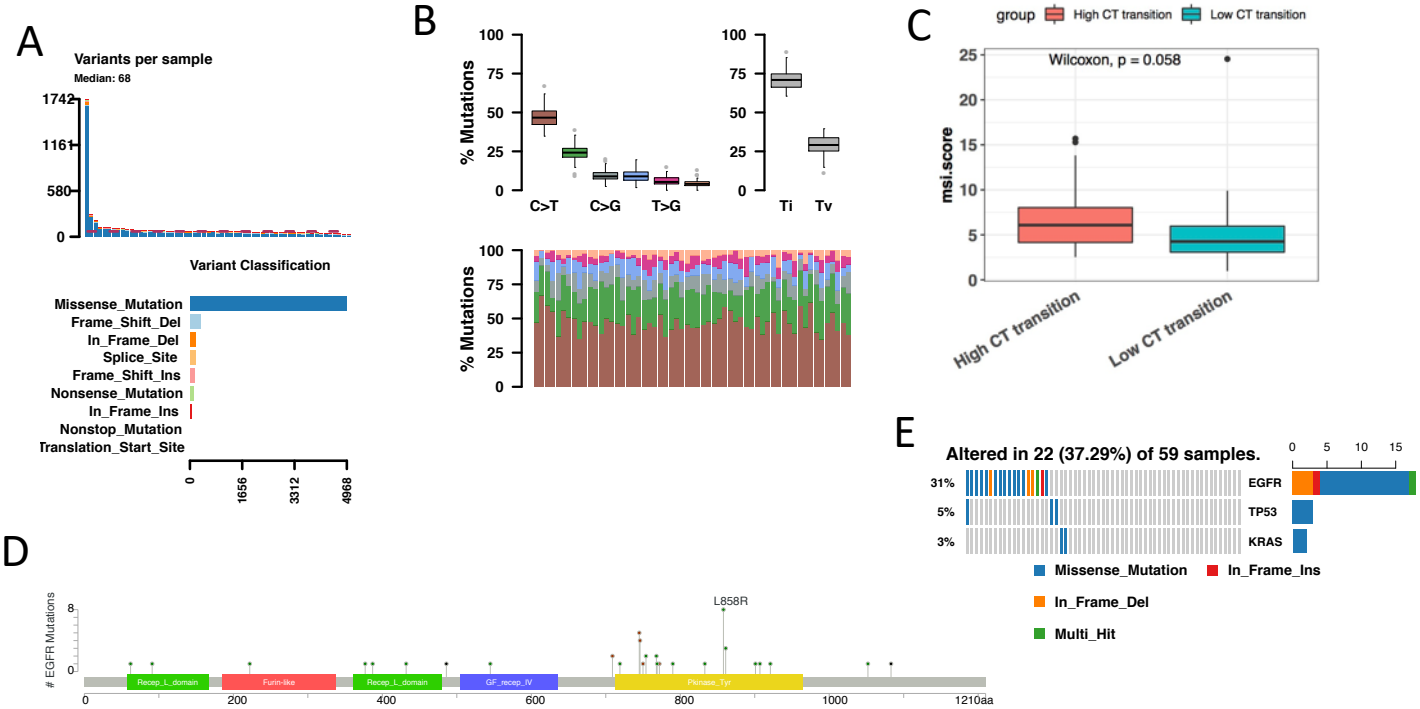
A
Variants per sample
Median: 68
1742
1161
580
0
Variant Classification
Missense_Mutation
Frame_Shift_Del
In_Frame_Del
Splice_Site
Frame_Shift_Ins
Nonsense_Mutation
In_Frame_Ins
Nonstop_Mutation
Translation_Start_Site
0
1656
3312
4968
B
% Mutations
C>T
C>G
T>G
Ti
Tv
C
group
High CT transition
Low CT transition
Wilcoxon, p = 0.058
msi.score
High CT transition
Low CT transition
E
Altered in 22 (37.29%) of 59 samples.
31%
5%
3%
EGFR
TP53
KRAS
Missense_Mutation
In_Frame_Ins
In_Frame_Del
Multi_Hit
D
EGFR Mutations
L858R
Recep_L_domain
Furin-like
Recep_L_domain
GF_recep_IV
Pkinase_Tyr
1210aa

Figure S5

A

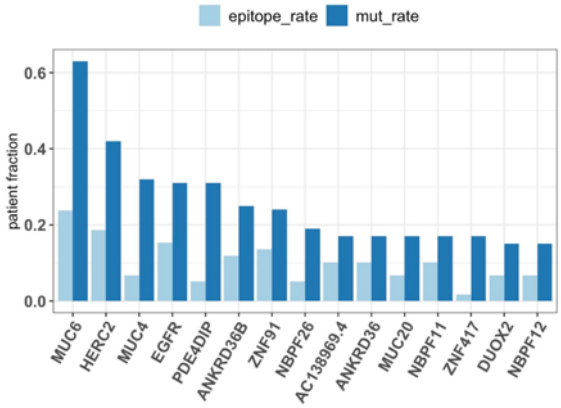
epitope_rate
mut_rate
patient fraction
0.6
0.4
0.2
0.0
MUC6
HERC2
MUC4
EGFR
PDE4DIP
ANKRD36B
ZNF91
NBPF26
AC138969.4
ANKRD36
MUC20
NBPF11
ZNF417
DUOX2
NBPF12

B

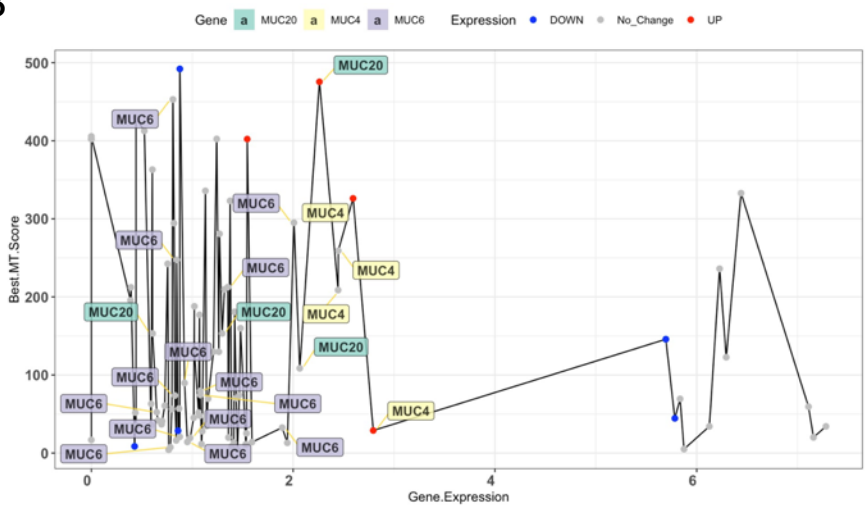
Gene
MUC20
MUC4
MUC6
Expression
DOWN
No_Change
UP
Best.MT.Score
Gene.Expression
500
400
300
200
100
0
0
2
4
6

Figure S6

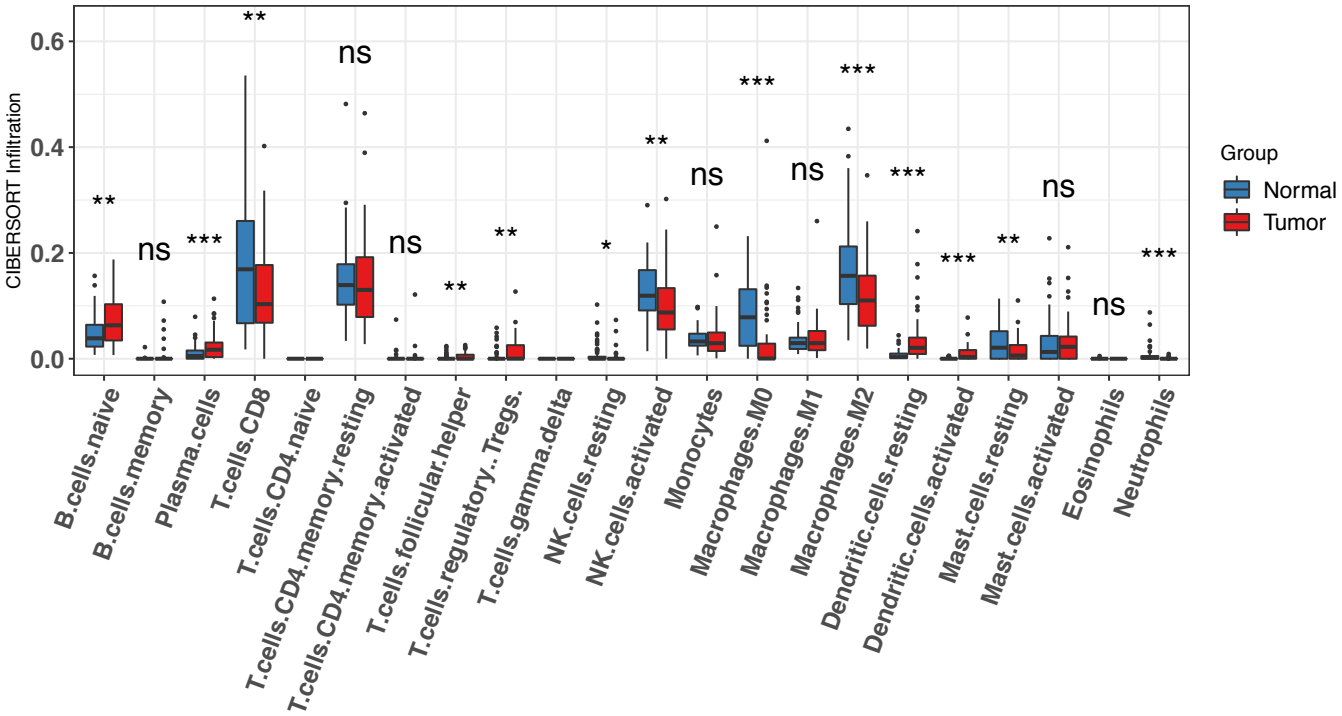
CIBERSORT Infiltration
0.6
0.4
0.2
0.0
**
ns
***
**
ns
ns
**
**
*
**
ns
***
ns
***
***
**
ns
ns
***
B.cells.naive
B.cells.memory
Plasma.cells
T.cells.CD8
T.cells.CD4.naive
T.cells.CD4.memory.resting
T.cells.CD4.memory.activated
T.cells.follicular.helper
T.cells.regulatory..Tregs.
T.cells.gamma.delta
NK.cells.resting
NK.cells.activated
Monocytes
Macrophages.M0
Macrophages.M1
Macrophages.M2
Dendritic.cells.resting
Dendritic.cells.activated
Mast.cells.resting
Mast.cells.activated
Eosinophils
Neutrophils
Group
Normal
Tumor

Figure S7

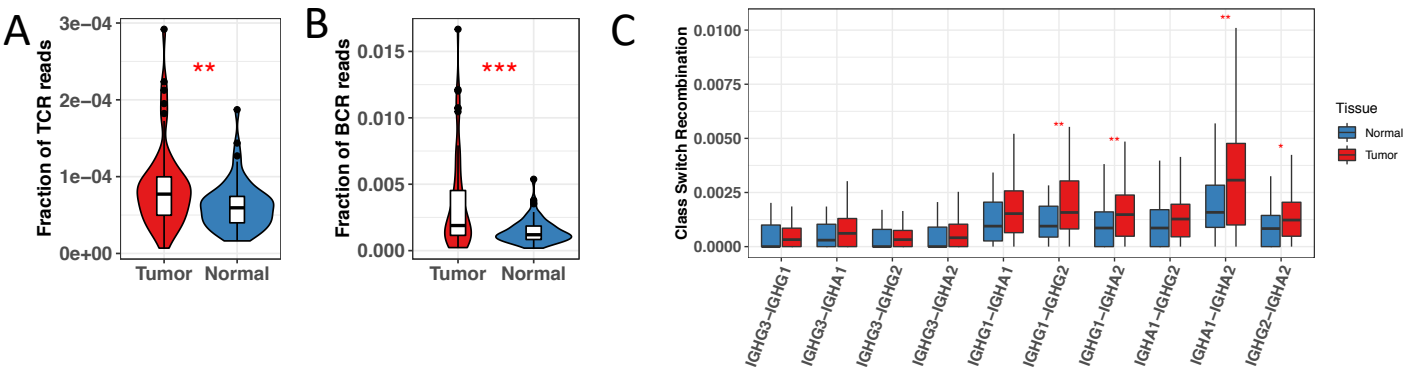
A
Fraction of TCR reads
3e−04
2e−04
1e−04
0e+00
**
Tumor
Normal
B
Fraction of BCR reads
0.015
0.010
0.005
0.000
***
Tumor
Normal
C
Class Switch Recombination
0.0100
0.0075
0.0050
0.0025
0.0000
IGHG3–IGHG1
IGHG3–IGHA1
IGHG3–IGHG2
IGHG3–IGHA2
IGHG1–IGHA1
IGHG1–IGHG2
IGHG1–IGHA2
IGHA1–IGHG2
IGHA1–IGHA2
IGHG2–IGHA2
Tissue
Normal
Tumor

Figure S8

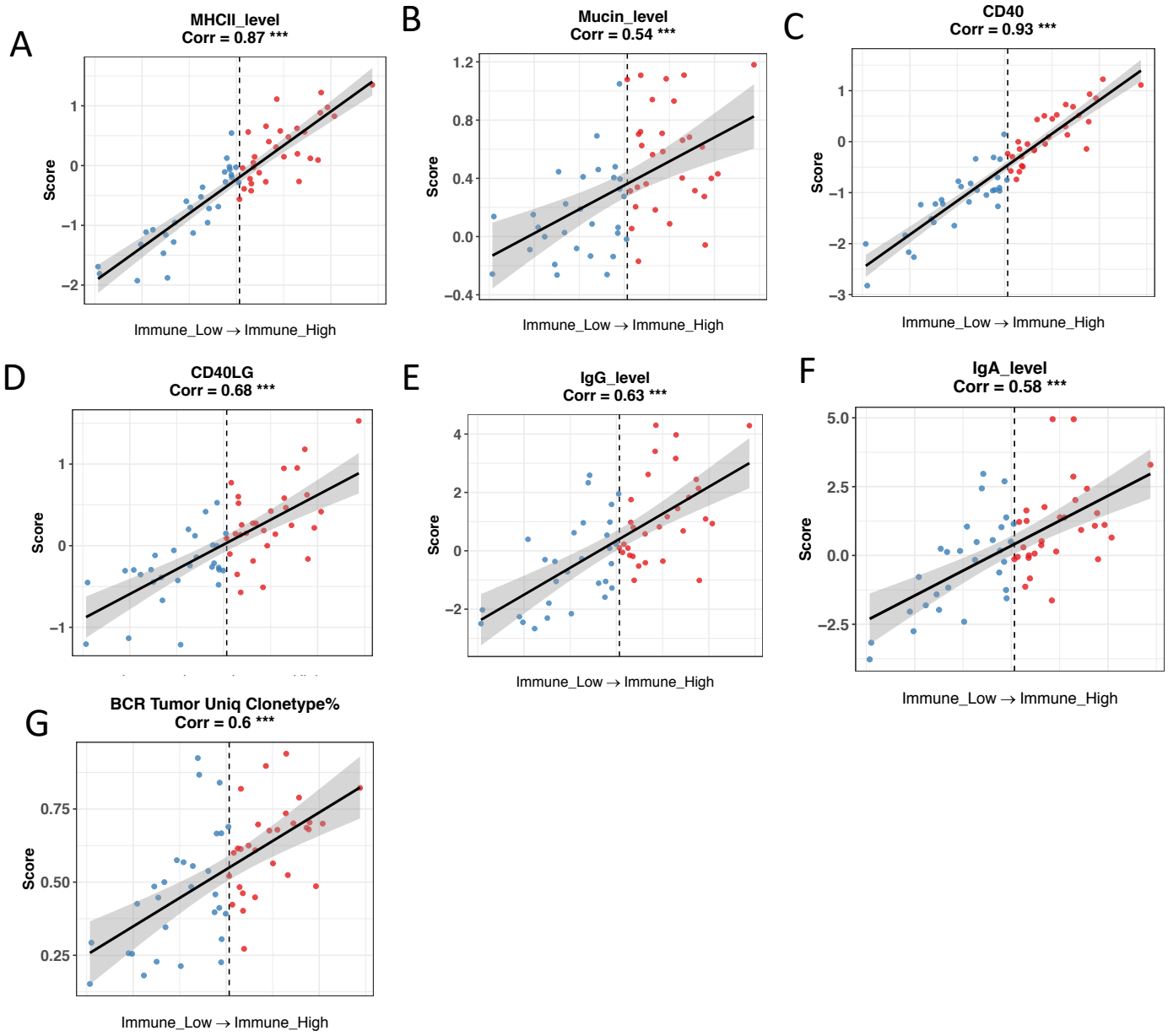
A
MHCII_level
Corr = 0.87 ***
Score
Immune_Low → Immune_High
B
Mucin_level
Corr = 0.54 ***
Score
Immune_Low → Immune_High
C
CD40
Corr = 0.93 ***
Score
Immune_Low → Immune_High
D
CD40LG
Corr = 0.68 ***
Score
E
IgG_level
Corr = 0.63 ***
Score
Immune_Low → Immune_High
F
IgA_level
Corr = 0.58 ***
Score
Immune_Low → Immune_High
G
BCR Tumor Uniq Clonetype%
Corr = 0.6 ***
Score
Immune_Low → Immune_High

Figure S9

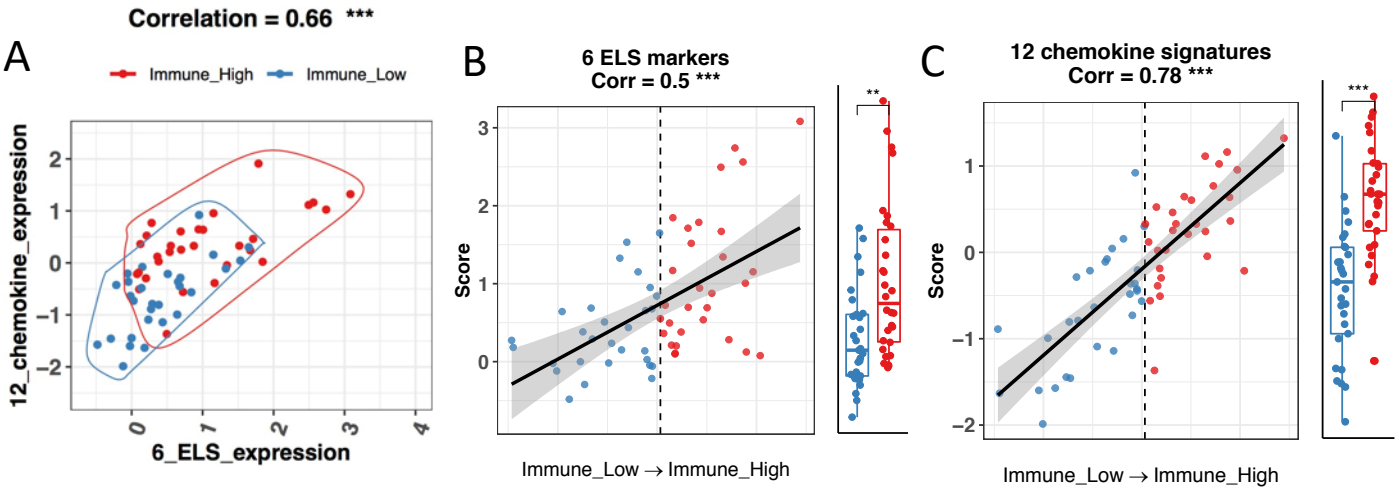
A
Correlation = 0.66 ***
Immune_High
Immune_Low
12_chemokine_expression
6_ELS_expression
B
6 ELS markers
Corr = 0.5 ***
Score
Immune_Low → Immune_High
**
C
12 chemokine signatures
Corr = 0.78 ***
Score
Immune_Low → Immune_High
***

Figure S10

A

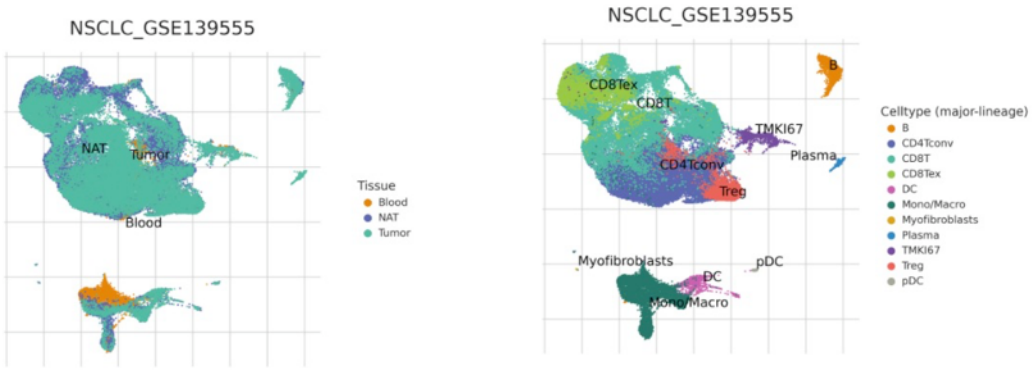

B

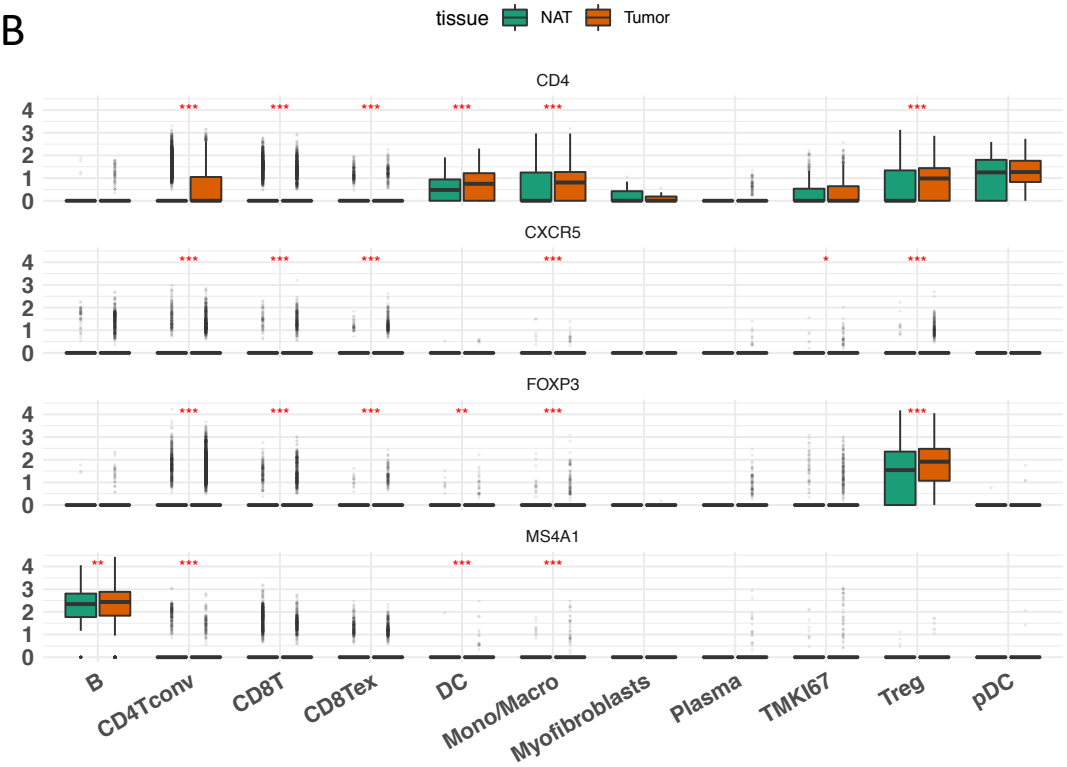

Figure S11

A

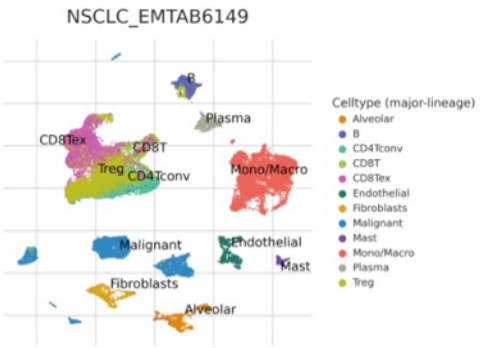

B

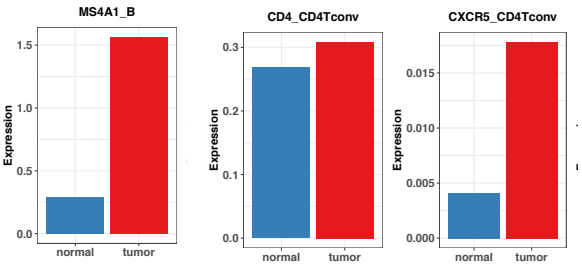

C

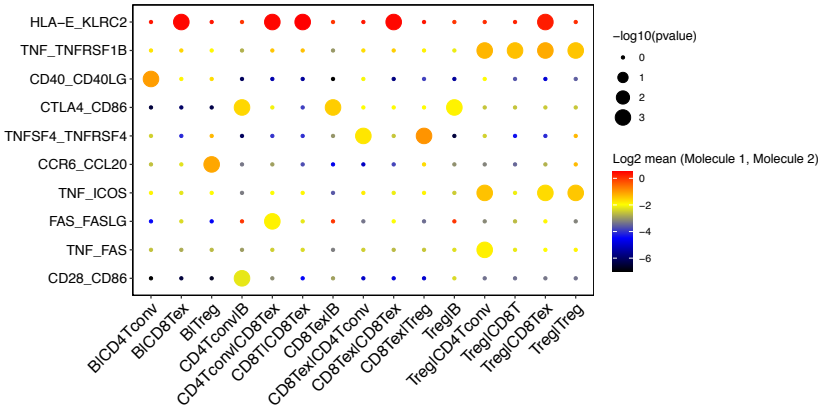

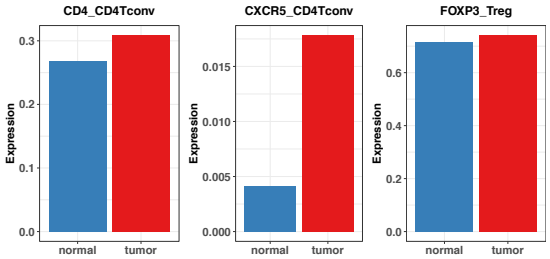

Figure S12

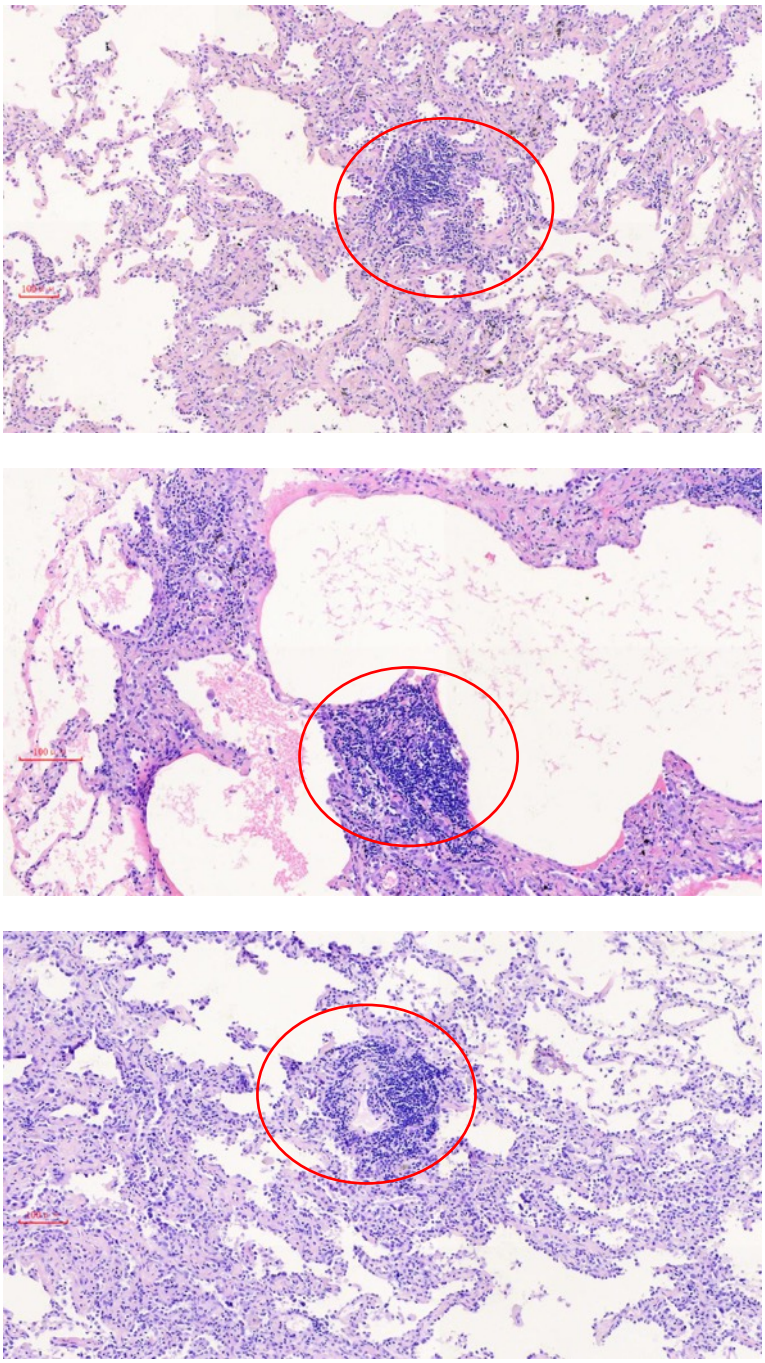

Figure S13

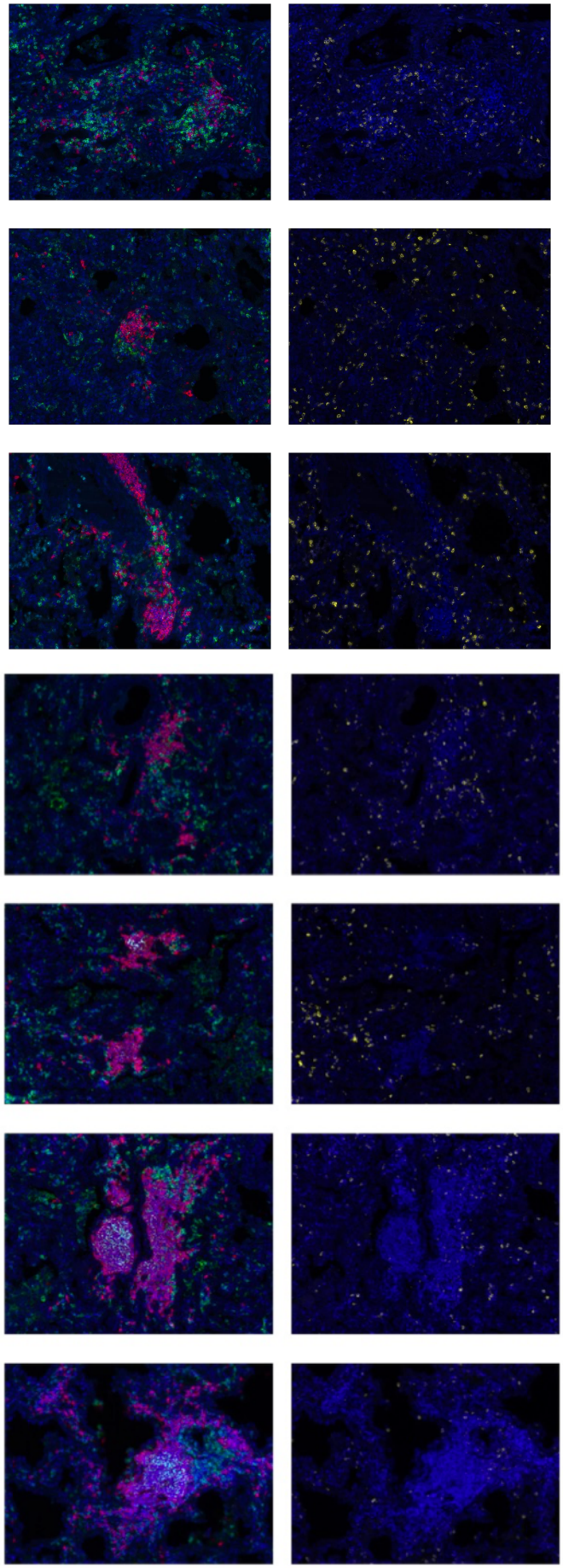

Figure S14

A

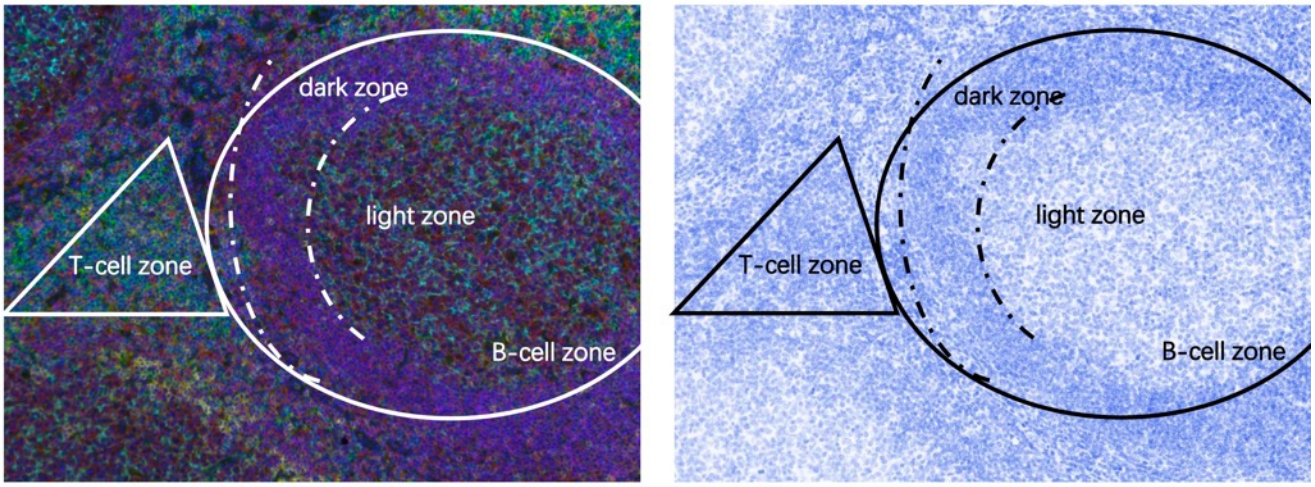

B

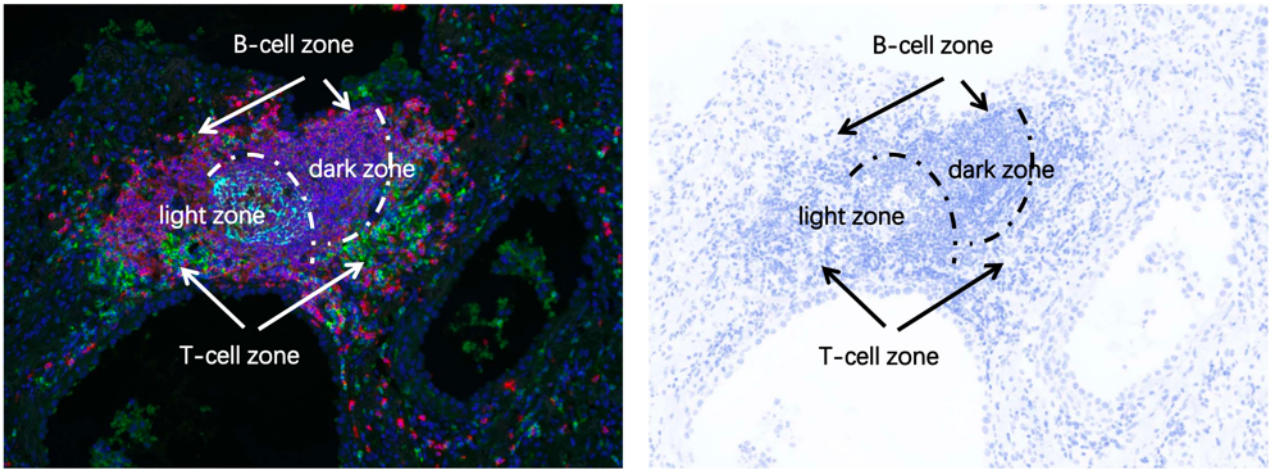

Figure S15

A

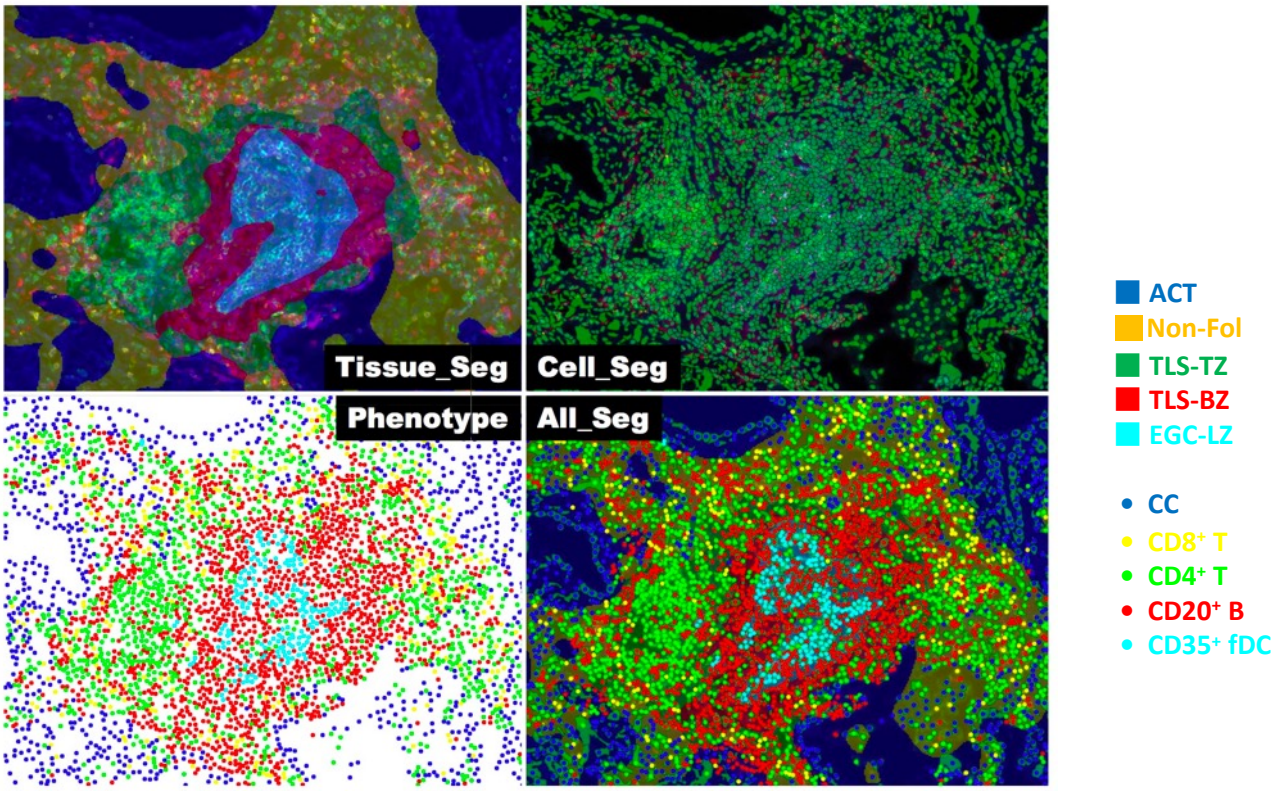

B

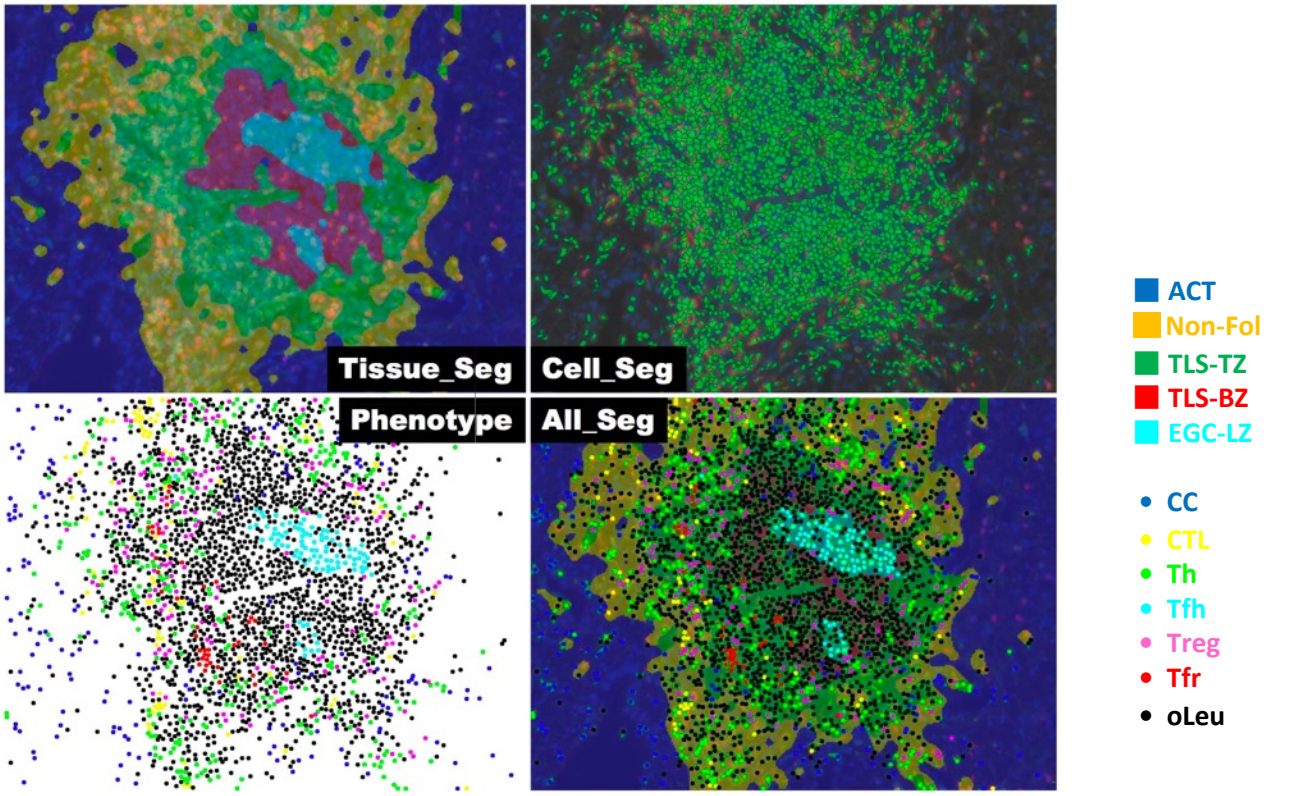

Figure S16

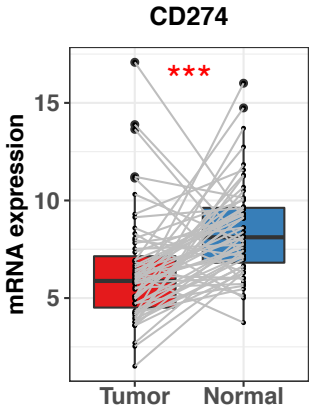
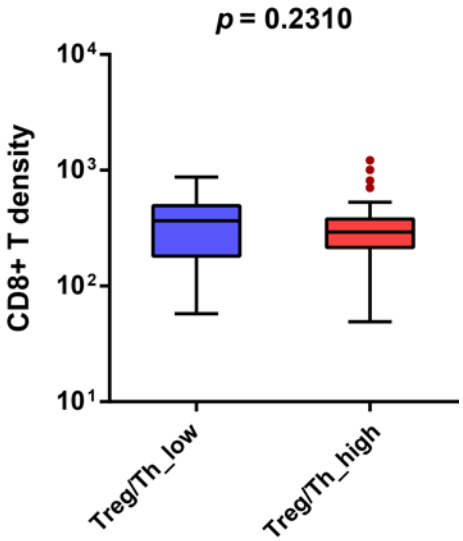
Figure S17